CHALMERS
UNIVERSITY OF TECHNOLOGY

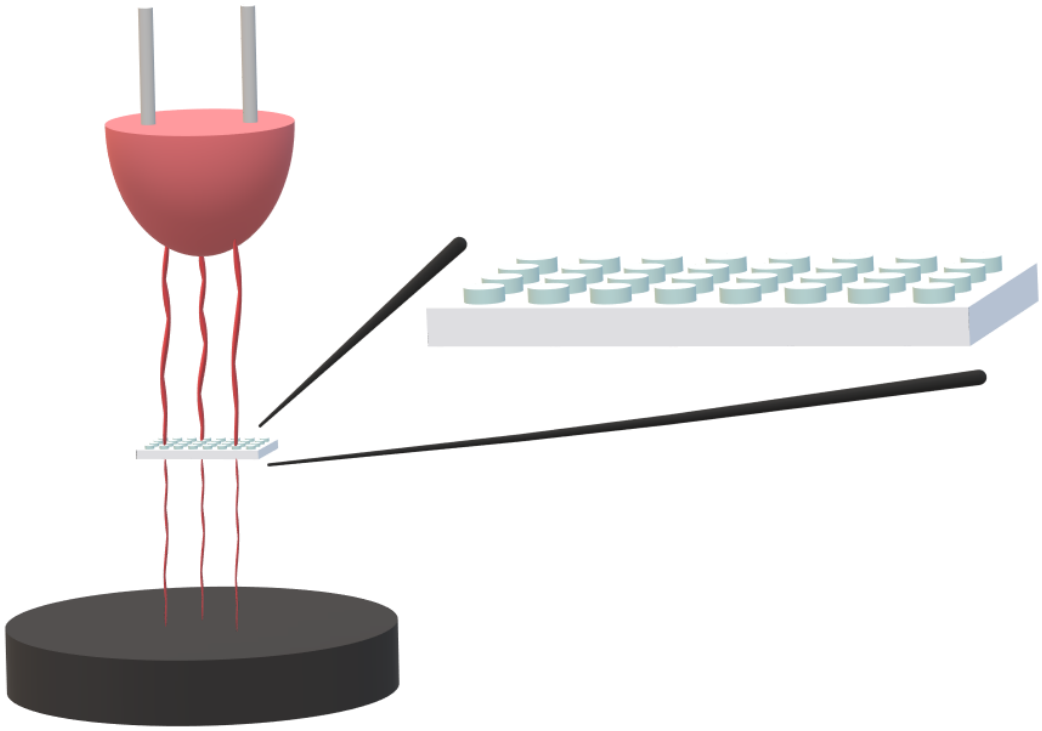

# Need for Speed

## Integrating the Worlds Fastest Hydrogen Sensor onto a Miniaturized Platform

Master's thesis in Applied Physics

BJÖRN LÖNN

Department of Applied Physics
CHALMERS UNIVERSITY OF TECHNOLOGY
Gothenburg, Sweden 2020

Master's thesis 2020

# Need for Speed

Integrating the Worlds Fastest Hydrogen Sensor onto a Miniaturized Platform

BJÖRN LÖNN




CHALMERS
UNIVERSITY OF TECHNOLOGY

Department of Applied Physics
*Division of Chemical Physics*
Chalmers University of Technology
Gothenburg, Sweden 2020

Need for Speed
Integrating the Worlds Fastest Hydrogen Sensor onto a Miniaturized Platform
BJÖRN LÖNN

© BJÖRN LÖNN, 2020.

Supervisor: Irem Tanyeli, Insplorion
Examiner: Christoph Langhammer, Department of Physics

Master's Thesis 2020
Department of Physics
Division of Chemical Physics
Chalmers University of Technology
SE-412 96 Gothenburg
Telephone +46 31 772 1000

Cover: Visualization of the nanoplasmonic hydrogen sensing technology, consisting of an LED light source, a photodiode detector and a glass substrate containing plasmonic nanodiscs.

Typeset in LaTeX
Printed by Chalmers Reproservice
Gothenburg, Sweden 2020

Need for Speed
Integrating the Worlds Fastest Hydrogen Sensor onto a Miniaturized Platform
BJÖRN LÖNN
Department of Physics
Chalmers University of Technology

# Abstract

The hydrogen revolution may finally be around the corner, with fuel cell driven vehicles and hydrogen gas turbines to mention just a few examples of applications. With such a transformation comes a need of fast and sensitive hydrogen detection systems. Nanoplasmonic hydrogen sensors have been a studied topic at Chalmers University for over a decade, and offer the fastest hydrogen sensing equipment to date. In order to become commercially attractive, the technology needs to be altered and integrated onto a platform consisting of cheap electronic components. This thesis demonstrates a first such attempt for a miniaturized nanoplasmonic hydrogen sensor, by combining the sensing technology developed at Chalmers, with Insplorion's low-cost NPS-platform. The optimized device developed here meets the requirements of detection range and accuracy, stated by the U.S. Department of Energy, but exhibits a response time considerably slower than what is required.

Keywords: hydrogen economy, hydrogen sensors, nanoplasmonic hydrogen sensing, sensor optimization, miniaturization, nanoplasmonic sensing (NPS)

# Acknowledgements

I would like to start by thanking the full team at Insplorion for some great couple of months. An extra appreciation goes to Irem, my supervisor, for all the help with sensor fabrication, insights and experiments. Olof, Martin and Per also deserve personal mentions for their efforts during my thesis. At Chalmers University, I want to thank my examiner Christoph Langhammer, for guidance and support, as well as Paul Erhart and Magnus Rahm for giving me access to their dielectric functions of PdAu-alloys. Finally, a shout-out to my fellow diploma students, Damien and Simon, it has been a fun time!

Björn Lönn, Gothenburg, June 2020

# Contents

**List of Figures** **xi**

**List of Tables** **xiii**

**1 Introduction** **1**
1.1 Hydrogen Economy . . . 1
1.2 Hydrogen Sensors . . . 1
1.3 Nanoplasmonic Hydrogen Sensing . . . 2
1.4 Advantages of LSPR Hydrogen Sensing . . . 3
1.5 Miniaturizing the Sensor . . . 3
1.6 Scope of the Thesis . . . 3
1.7 Limitations . . . 4

**2 Theory** **5**
2.1 Plasmons . . . 5
2.1.1 LSPR . . . 6
2.1.2 Quasi-static Approximation of Oblate Spheroids . . . 7
2.2 Metal Hydrides . . . 9
2.2.1 Hydride Formation . . . 9
2.2.2 Hysteresis . . . 10
2.2.3 Metal-Hydride LSPR Hydrogen Sensing . . . 11
2.3 Hydrogen Sensing in the LUFT-device . . . 12

**3 Methods** **13**
3.1 Simulations . . . 13
3.2 Experimental . . . 13
3.2.1 Sensor Chip Manufacturing . . . 13
3.2.2 Measurements in the Chalmers Reactor Setup . . . 14
3.2.3 Measurements in the LUFT-device . . . 15
3.3 Plotting and Data Analysis . . . 17

**4 Results & Discussion** **19**
4.1 Simulations . . . 19
4.1.1 Optimal Wavelength for Hydrogen Sensing . . . 19
4.2 Experiments at the Chalmers Reactor . . . 21
4.2.1 Optimal Wavelength for Hydrogen Sensing . . . 21
4.2.2 Achievable Extinction Change . . . 22

4.2.3 Response Time Evaluation . . . . . 24
4.3 Experiments with the LUFT-device . . . . . 25
4.3.1 940 nm LEDs . . . . . 25
4.3.2 650 nm LEDs . . . . . 27
4.3.3 Calibration Curves for the LUFT-device . . . . . 29

**5 Conclusion** **31**
5.1 Future Work . . . . . 31

**Bibliography** **33**

**A Appendix 1** **I**
A.1 Matlab Scripts and Functions Used for Simulations . . . . . I
A.1.1 Script Used for Comparing Simulations and Experimental Results . . . . . I
A.1.2 Function (newrefrac) Used in the A.1.1 Script . . . . . VI
A.1.3 Script for Calculation of LSPR Response from Differently Alloyed Nanoparticles . . . . . VIII
A.2 Matlab Scripts for Evaluation of Experiments in the Reactor and the LUFT-device . . . . . XII
A.2.1 Script for Visualising Experimental Data from the LUFT-device or the Reactor . . . . . XII
A.2.2 Function (absoluteShift) Used to Extract Changes in Extinction and Transmission . . . . . XIII
A.2.3 Calibration Curve Constructing Script . . . . . XIII

# List of Figures


2.1 The two different kinds of surface plasmons. In a) a so-called surface plasmon polariton, propagating at the interface between a metal and a dielectric. In b) a localized surface plasmon, confined to a spherical nanoparticle, taking the form of an oscillating dipole. . . . . 5

2.2 Palladium hydride formation. Molecular hydrogen incident on the palladium surface are dissociated into atomic hydrogen, with the metal acting as a catalyst. The atomic hydrogen diffuse into the lattice and occupies the interstitial sites. . . . . 9

2.3 An illustration of an $\alpha$-phase (low hydrogen pressures) is shown in the left column. Similarly, the coexistence region (plateau pressure) consisting of both $\alpha$- and $\beta$-phases, and the pure $\beta$-phase (high hydrogen pressures), are shown in the middle and right columns, respectively. . 10

2.4 Pressure-composition isotherms of materials exhibiting a) hysteresis, b) suppressed hysteresis. Red arrows correspond to $\beta$-phase formation and black arrows to $\beta$-phase decomposition. . . . . 11

2.5 Plasmon peaks of a metal (black) and its related metal hydride (red), illustrating the peak shift caused by hydride formation. The read-out signals $\Delta\lambda_{LSPR}$, $\Delta\text{Ext}_{peak}$ and $\Delta\text{Ext}$ are indicated by gray bars. The spectral region marked in blue highlights low-signal sensing region when using the $\Delta\text{Ext}$ read-out. . . . . 12

3.1 Schematic of the *Insplorion X1* instrument. Gas enters through the gas inlet connection seen to the right. It is transported passed the sensor chips and exits through the outlet connection to the left. The collimating lenses allowed fiber optic connections to and from the light source and detector. . . . . 15

3.2 Schematic of the LUFT-device. Gas enters at the inlet to the left, then passes through the empty volume until it reaches the sensing area around the sensor chip. The photodiode detector registers the change in transmission of light as hydride formation takes place in the nanoparticles on the sensor chip. . . . . 16

3.3 Response curve of the photodiode detector. . . . . 17

4.1 Extinction cross sections (simulation) and extinction (experimental) as a function of wavelength, for two different hydrogen concentrations, 0% (solid) and 4% (dashed). . . . . 19

4.2 ΔExt (experimental) and $\Delta\sigma_{ext}$ (simulation) due to an increase in hydrogen concentration from 0% to 4%. Optimum and non-optimum sensing regions are observed in both curves, with spectral offsets between simulation and experimental results. . . . . 20
4.3 ΔExt for 4% hydrogen, highlighting the two optimum sensing regions around 715 nm and 940 nm (maxima), alongside the non-optimal sensing region centered around 830 nm (minima). . . . . 21
4.4 Extinction caused by an array of 210x25 nm $Pd_{80}Au_{20}$ nanoparticles on a glass substrate, measured at two different wavelengths, for different hydrogen concentrations in argon. . . . . 22
4.5 Relative transmission changes from reactor measurements, caused by an array of 210x25 nm $Pd_{80}Au_{20}$ nanoparticles on a glass substrate, measured at three different wavelengths, for different hydrogen concentrations in argon. . . . . 23
4.6 Relative extinction change from measurements in the LUFT-device, using 940 nm LEDs as light source, for hydrogen concentrations in the range of 0.01% to 4%. . . . . 25
4.7 Relative transmission changes from measurements in the LUFT-device, using 650 nm LEDs as light source, for hydrogen concentrations in the range between 0.01% to 4%. . . . . 27
4.8 Calibration curve of the LUFT-device equipped with 650 nm and 940 nm LEDs. Shown is the relative transmission changes, plotted versus hydrogen concentration (%), on a log scale. . . . . 29

# List of Tables


4.1 Absolute extinction change for a range of $H_2$ concentrations, measured at 715 nm and 940 nm wavelengths, using the Chalmers reactor setup. 23
4.2 Relative transmission change for a range of $H_2$ concentrations, measured at 650, 715 and 940 nm wavelengths using the Chalmers reactor setup. . . . . 24
4.3 Response times from experiments in the Chalmers reactor setup. . . . 24
4.4 Mean relative transmission changes and their standard deviations in the LUFT-device, using 940 nm LEDs. . . . . 25
4.5 Mean relative transmission changes and their standard deviations in the LUFT-device, using 940 nm LEDs with improved mounting of the sensor chip. . . . . 26
4.6 Response times ($t_{90}$), from measurements done in the LUFT-device, for a range of hydrogen concentrations in argon gas. . . . . 27
4.7 Mean relative transmission changes and their standard deviations, using 650 nm LEDs . . . . . 28

# 1
# Introduction

This chapter introduces the concept of LSPR hydrogen sensing. It also includes a brief background on the hydrogen economy, hydrogen sensing applications and existing technology. At the end of the chapter the scope of the thesis is explained and put into this context.

## 1.1 Hydrogen Economy

In a time when the effects of climate change and global warming are becoming increasingly evident, scientists, politicians and society as a whole need to unite and cooperate to overcome the grand challenges humanity are facing. There is not one single answer that will provide the complete solution, but an important part lies in the transition from a fossil fuel based energy system, towards one based on renewable sources. The **Hydrogen Economy** has been proposed as one such transition path.[1] By using hydrogen as an energy carrier and fuel cells or combustion engines for energy conversion, it is possible to run transportation, industrial processes, domestic heat and power supplies with minimal $CO_2$ emissions, if the energy needed for hydrogen production is provided from renewable sources.[1][2] The application areas of hydrogen are numerous and not restricted to the hydrogen economy. Already today hydrogen is commonly found as a component in, or as an end- or by-product in chemical industries.[3]

## 1.2 Hydrogen Sensors

It is a widely known fact that hydrogen gas cause a large explosion risk when mixed with air. Its flammability range covers a wide spread of concentrations, from 4 vol% to 75 vol% at ambient conditions.[4] Due to these reasons, fast and sensitive hydrogen sensors are of utmost importance in order to face the safety issues associated with hydrogen related applications.

The U.S. Department of Energy (DOE) have compiled a list of target requirements for hydrogen sensors. These have been summarized by Buttner et al.[5] and are listed below:

- Detection range: 0.1-10%
- Accuracy: 5% of full scale
- Response time: <1s
- Gas environment: Ambient air (relative humidity 10-98%)

- Operating temperature: -30 to 80°C
- Lifetime: 10 years
- Interference: Resistance (e.g., hydrocarbons)

Naturally, high accuracy and a broad detection range are important factors for a hydrogen safety sensor, and a fast response time is necessary due to the flammable nature of hydrogen gas. Furthermore, the sensor should be able to operate at ambient conditions during a long period of time, to minimize the need for maintenance.

There are numerous different technologies for hydrogen sensing commercially available today. These include, among others, electrochemical-, metal oxide-, thermal conductivity- and Pellistor-type combustible gas-sensors. While each technology has its own advantages, none of them manage to fulfill all the requirements. The shortcomings are, for most of them, low selectivity, meaning that the sensors are unable to differentiate between the targeted gas, in this case hydrogen, and one or more contaminant gases that may be present. This type of cross-sensitivity is naturally not desirable when developing a gas sensor for hydrogen detection. Another problem for some of the existing technologies, including the electrochemical sensors, are slow response times on the order of minutes rather than seconds.[5] Hence, there is need for an improved technology, new or old, that meets all the requirements.

## 1.3 Nanoplasmonic Hydrogen Sensing

For well over a decade, a hydrogen sensor technology based on **localized surface plasmon resonance** (LSPR), has been developed by a research group at Chalmers University of Technology. In 2019, the group published a paper demonstrating the fastest reported hydrogen sensor for hydrogen pressures in the range of 1-100 mbar.[6] The complete theory behind LSPR as a physical phenomenon and its utilization as a means of sensing technology is quite extensive and will be discussed on a more detailed level in the upcoming Theory chapter. However, it is necessary to already now give the reader an understanding of the processes involved in nanoplasmonic hydrogen sensing.

**Localized urface plasmon resonance** is a physical phenomenon occurring in metallic nanoparticles. Light that is directed onto the nanoparticles can, if its wavelength is larger than the particles, excite resonant collective oscillations of the nanoparticles conduction electrons, a so called LSPR. At this resonant wavelength, the absorption and scattering efficiencies of the nanoparticles are highly increased. What determines the resonant wavelength is a combination of nanoparticle shape, size and optical properties, as well as the optical properties of the surrounding. This opens up opportunities for hydrogen sensing.[3]

Being the lightest element, atomic hydrogen possess the ability to diffuse into a metal lattice to occupy the interstitial sites between the metal atoms. This process creates a new material, namely a metal hydride, where the hydrogen concentration within the hydride depends on the hydrogen pressure outside the particle. Such a change of phase results both in a change in optical properties and volume expansion,

of the nanoparticle. Hence, it will therefor also affect the LSPR wavelength, and by tracking this change it is possible to perform accurate and fast detection of hydrogen.[3]

## 1.4 Advantages of LSPR Hydrogen Sensing

There are several reasons why LSPR hydrogen sensors are to prefer over existing technology. As mentioned, most of the standard technologies suffer from low selectivity and some from slow response times.[5] Both these issues can be overcome when using LSPR techniques, as demonstrated by researchers at Chalmers.[6] Their work shows that certain polymer coatings protect the sensing particles from interfering gases, thereby increasing selectivity. At the same time, it promotes the kinetics of hydride formation. Another advantage is that the risk of creating sparks is completely removed in LSPR sensing, a most important feature due to the flammable nature of hydrogen-air mixtures.[3] Furthermore, by varying for example size, shape and alloying of the nanoparticle, it is possible to tune the LSPR peak to basically any desired wavelength in the visible range. The high sensitivity and the possibility of technology miniaturization are two other key advantages, where the latter also generates some challenges related to sensor-device integration and optimization.

## 1.5 Miniaturizing the Sensor

As it has been demonstrated at Chalmers [6], the LSPR hydrogen sensor performs exceptionally well in a highly controlled laboratory environment, using expensive and bulky equipment. For the technology to become commercially attractive for applications mentioned earlier in this chapter, there is however, a need to miniaturize the technology using smaller and cheaper components. Replacing for example the white light source and spectrometer detector in the laboratory setup with a monochromatic LED light source and a photodiode detector results in a decrease in both size and cost of the device. Such changes would, however, change the performance of the sensor device. It still remains to be determined how well the technology would perform when implemented on a low-cost sensor chip such as Insplorion's NPS-platform, and how it could be optimized.

## 1.6 Scope of the Thesis

Within this project, focus will be put on the performance of the technology developed at Chalmers, when integrated with Insplorion's sensing platform, specifically their sensing device named *LUFT*, and how to improve it. An effort will be made to simulate the LSPR response of nanoparticles of different size, aspect ratio and alloying. In addition, a simplified method of simulating hydrogen presence is introduced and evaluated. The simulation part is performed both to gain a deeper understanding of the theory behind LSPR and to aid the decisions regarding nanoparticle size, alloying, aspect ratio and LED wavelength during device optimization. The sensors

will be evaluated experimentally both at a Chalmers reactor setup and in the miniaturized sensor device (LUFT) to compare their performances. At the end, the goal is to have a device displaying high sensitivity towards hydrogen, for a wide range of concentrations.

## 1.7 Limitations

As already mentioned, this thesis is about the performance of the LUFT-device, when equipped with the Chalmers-developed hydrogen sensors. Therefor, to avoid that too much time is spent evaluating different nanoparticle sizes and aspect ratios, a maximum of three different sizes was decided at the beginning, where the most promising one was to be used in the LUFT-device. Regarding LEDs in the device, two wavelengths were assessed in the LUFT-device. These were as a consequence, chosen carefully based on experimental results. The time at hand was to decide if any coatings were to be examined. If time had allowed, the most interesting ones were PMMA and PTFE [6], however, the fabrication of a PTFE coating was not viable at the time of this project, which left PMMA as the sole candidate of such a scenario.

# 2

# Theory

This chapter aims to explain enough of the theory describing plasmons, metal hydrides and LSPR hydrogen sensing to ensure that the reader understands the full content of the thesis, as well as its relevance for future applications.

## 2.1 Plasmons

As briefly mentioned in the Introduction chapter, plasmons are a physical phenomena occurring in metals and some dielectrics, so called plasmonic materials. They are defined as the quantum of plasma oscillations, the collective oscillations of the material's conduction electrons, resulting from an applied electromagnetic field.[7] Plasmons can be divided into three different kinds based on their environment; bulk, surface and localized surface plasmons (LSP). Of interest here are the surface plasmons and in particular, the localized surface plasmons. At the interface between a plasmonic material and a dielectric, plasmons appear as charge density fluctuations, either propagating along the surface in the case of surface plasmons, also called surface plasmon polaritons (SPP), or as localized surface plasmons if they are confined to a nanoparticle. Figure 2.1 illustrates the difference between the two types of surface plasmons.

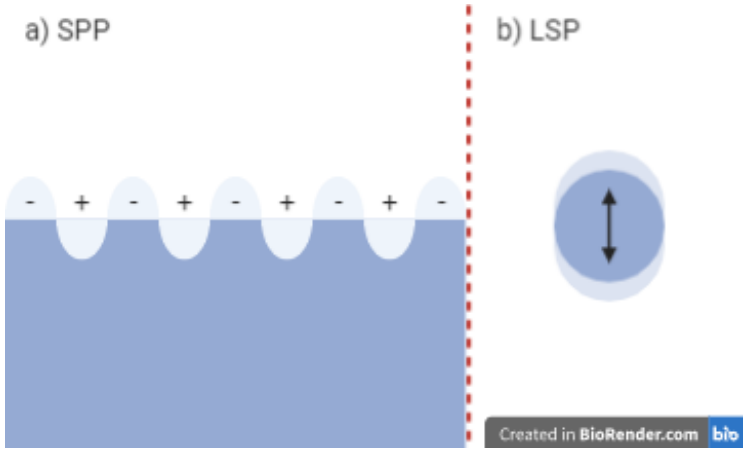


**Figure 2.1:** The two different kinds of surface plasmons. In a) a so-called surface plasmon polariton, propagating at the interface between a metal and a dielectric. In b) a localized surface plasmon, confined to a spherical nanoparticle, taking the form of an oscillating dipole.

Surface plasmons possess the ability to couple with photons.[8] In fact, plasmon modes in many of the noble metals can be excited by light in the visible range, or for wavelengths close to visible. Such excitations are what give rise to the intriguing phenomenon of LSPR in metal nanoparticles.

### 2.1.1 LSPR

When the plasmon modes of a noble metal nanoparticle are excited by white light, for a specific wavelength within this polychromatic light, the excited plasma oscillations will become resonant.[9] The phenomenon is called localized surface plasmon resonance (LSPR) and around the resonance frequency, the nanoparticle absorbs and scatters light with higher efficiency compared to other wavelengths, leading to a peak in its extinction spectrum.[7]

The underlying theory of LSPR is extensive and mathematically complex, but to get a brief understanding of the processes involved one can start by looking at the theory developed by Gustav Mie in the beginning of the 20th century.[10] By solving Maxwell's equations for a plane wave, incident on a homogeneous, conducting sphere, Mie was able to find an analytical expression for the extinction cross-section, as described by equation 2.1. The extinction cross-section has the unit $nm^2$. Hence, it is actually an area, but should be thought of as a measure of probability for extinction of the incident photons.

$$\sigma_{ext} = \frac{2\pi}{|k|^2} \sum_{L=1}^{\infty} (2L+1)[Re(a_L + b_L)] \tag{2.1}$$

In equation 2.1, the wavevector of the incoming light is represented by k, and L are integers corresponding to the different multipoles of the scattering (i.e. dipoles, quadrupoles etc.). Furthermore, $a_L$ and $b_L$ are parameters described by equation 2.2 and 2.3 respectively, composed of the Ricatti-Bessel functions $\psi_L$ and $\chi_L$.

$$a_L = \frac{m\psi_L(mx)\psi'_L(x) - \psi'_L(mx)\psi_L(x)}{m\psi_L(mx)\chi'_L(x) - \psi'_L(mx)\chi_L(x)} \tag{2.2}$$

$$b_L = \frac{\psi_L(mx)\psi'_L(x) - m\psi'_L(mx)\psi_L(x)}{\psi_L(mx)\chi'_L(x) - m\psi'_L(mx)\chi_L(x)} \tag{2.3}$$

In the above equations, $m = \tilde{n}/n_m$ is the fraction of the complex refractive index of the sphere, $\tilde{n} = n_R + in_I$, and the surrounding medium's real valued refractive index, $n_m$. The variable $x = k_m r$ is composed of $k_m$, the wavenumber in the medium and $r$, the particle radius.

The rather complex expression for the extinction cross-section in equation 2.1 can be simplified significantly by assuming the nanoparticles to be much smaller than the wavelength of the incoming light. Such a scenario corresponds to $x << 1$. The functions $\psi_L$ and $\chi_L$ can then be expanded as power series, and by discarding terms of order higher than $x^3$, much simpler expressions, however approximations, are found for $a_1$ and $b_1$, while higher order parameters are zero[7]:

$$a_1 \approx -\frac{i2x^3}{3}\frac{m^2-1}{m^2+2} \tag{2.4}$$

$$b_1 \approx 0 \tag{2.5}$$

Recalling that $m = (n_R + in_I)/n_m$, and using the expressions for the complex dielectric function of the sphere, $\tilde{\epsilon} = \epsilon_1 + i\epsilon_2$ where $\epsilon_1 = n_R^2 - n_I^2$ and $\epsilon_2 = 2n_R n_I$, and the dielectric function of the medium, $\epsilon_m = n_m^2$, $a_1$ can be expressed as[7]:

$$a_1 = -\frac{2x^3}{3}\frac{-i\epsilon_1^2 - i\epsilon_1\epsilon_m + 3\epsilon_2\epsilon_m - i\epsilon_2^2 + i2\epsilon_m^2}{(\epsilon_1 + 2\epsilon_m)^2 + \epsilon_2^2} \tag{2.6}$$

Finally, substituting this expression for $a_1$ into equation 2.1 and neglecting terms other than the dipole, one arrives at the following simplified extinction cross-section expression[7]:

$$\sigma_{ext} = \frac{18\pi\epsilon_m^{3/2}V}{\lambda}\frac{\epsilon_2(\lambda)}{(\epsilon_1(\lambda) + 2\epsilon_m)^2 + \epsilon_2(\lambda)^2} \tag{2.7}$$

In this expression, valid for very small spherical nanoparticles (sizes up to 10nm) with volume $V$, the dependence of the extinction peak on the metal dielectric function becomes evident. The resonance wavelength corresponds to where the extinction cross-section is maximized. This happens when the denominator of equation 2.7 is minimized, hence the resonance condition for such a situation is $\epsilon_1(\lambda) = -2\epsilon_m$. The location of the resonance wavelength on the light spectrum, is thereby determined by the real part of the dielctric function. The imaginary part of the dielectric function on the other hand, is responsible for the damping losses, resulting in a broadening of the LSPR peak.[7] Small values for $\epsilon_2$ correspond to low losses, and hence a more narrow LSPR peak.

### 2.1.2 Quasi-static Approximation of Oblate Spheroids

This simplified example of LSPR in extremely small spheres is a great help in understanding the physics behind the phenomenon. However, for more complex geometries and larger nanoparticle sizes, the theory becomes more complicated. To serve the purposes of this thesis, it is important to find a theoretical model that allows sufficiently accurate simulations of the LSPR response of disc-shaped nanoparticles with sizes in the range of approximately 100-300nm. Here, sufficiently accurate refers to the ability to predict the LSPR response of a nanoparticle, given its dielectric function, in different surroundings. Hence, it should be able to accurately predict, for example, the resonance wavelength and give reasonable peak broadening.

The model chosen is the one used by Langhammer et al.[11], following the conventions and notations of Bohren and Huffman.[12] In this model, the nanodiscs are approximated by oblate spheroids and, again, the particles are assumed to be smaller than the wavelength of the incident light. Using such an approximation, denoted as the **Quasi-static approximation**, particles are treated as dipoles that has been

induced by an external field. In this case, it is assumed that the light is directed perpendicular onto one of the flat sides of the nanodisc. For the corresponding oblate spheroid this means parallel to its minor axis, resulting in a field that is parallel to its major axis. Then, the spheroid will possess a dipolar polarizability described in equation 2.8:

$$\alpha(\lambda) = \frac{\pi d^2 h}{6} \frac{\tilde{\epsilon}(\lambda) - \epsilon_m}{\epsilon_m + L(\tilde{\epsilon}(\lambda) - \epsilon_m)} \tag{2.8}$$

In equation 2.8, the first term is nothing else than the volume of a nanodisc, of height $h$ and diameter $d$. The factor $L$ in the second term, is a geometric factor related to the ratio of the major and minor particle axes. For a sphere, where all the axes have the same length, $L = 1/3$. However, for an ellipsoid, the three principal axes are of different length, meaning that there will be one distinct $L_i$ for each principal axis [13], given by equation 2.9:

$$L_i = \frac{a_1 a_2 a_3}{2} \int_0^\infty \frac{dq}{(a_i^2 + q) f(q)} \tag{2.9}$$

As $i = 1, 2, 3$ denotes the particle axes in the x-, y- and z-direction, respectively, $\{a_i\}$ are the lengths of the corresponding semi axes. In this expression, $f(q) = \sqrt{(q + a_1^2)(q + a_2^2)(q + a_3^2)}$. Note that for an oblate spheroid, the semi axes $a_1$ and $a_2$ have the same length, which simplifies equation 2.9 and results in only two distinct values for $L$, from now on denoted as $L_{xy}$ and $L_z$. These two values of $L$ in fact belong to two spectrally separated plasmon resonances that are a consequence of plasma oscillations along either the major or minor particle axis.[13] In our case, we only consider light incident on the particle in the z-direction, meaning that the oscillations will be along the major axis in the x-y plane, hence only $L_{xy}$ will come into play.

For nanoparticles with diameters in the range of 100-300nm, their size start to affect the plasmon resonance in other ways. For example, as the particle size increases, so does the radiation damping where the plasmons decay radiatively into photons. Other effects that arise are retardation of the exciting field across the volume as well as the depolarization field inside the particle.[13] Such finite wavelength effects need to be corrected, and here the correction used is the same as in [11]:

$$\alpha'(\lambda) = \alpha(\lambda) \left[ 1 - i\frac{k^3}{6\pi}\alpha(\lambda) - \frac{k^2}{2\pi d}\alpha(\lambda) \right]^{-1} \tag{2.10}$$

The corrected polarizability $\alpha'(\lambda)$ contains a $k^3$-term and a $k^2$-term which correct for the radiation damping and the dynamic depolarization, respectively, with $k$ being the wave vector of the light.[11] Finally, to conclude the model, the extinction cross-section is found from the imaginary part of the corrected polarizability by:

$$\sigma_{ext} = kIm[\alpha'(\lambda)] \tag{2.11}$$

## 2.2 Metal Hydrides

A metal hydride is, as its name suggests, a material composed of metal and hydrogen atoms. More specifically, the material structure consist of a metallic crystal lattice, where hydrogen atoms occupy the interstitial sites of the lattice. There exist numerous metal hydrogen systems, the most famous and longest studied one being palladium hydride (H-Pd), due to its low activation energy for hydrogen absorption.[14] The application areas for metal hydrides are equally diverse, including among others, hydrogen storage, batteries, catalysis and hydrogen sensing.[15]

### 2.2.1 Hydride Formation

For a metal hydride to form, the molecular hydrogen needs to dissociate into atomic hydrogen and subsequently become absorbed in the metal. Figure 2.2 shows the dissociation and diffusion steps during hydrogen absorption in a palladium lattice. In step 1 the molecular hydrogen approaches the metal surface. The metal then acts as a catalysts in the hydrogen dissociation reaction, yielding atomic hydrogen as depicted in step 2. In the third and last step, hydrogen atoms diffuse into the lattice, until they reach vacant interstitial sites, displayed in figure 2.2 as dashed circles.

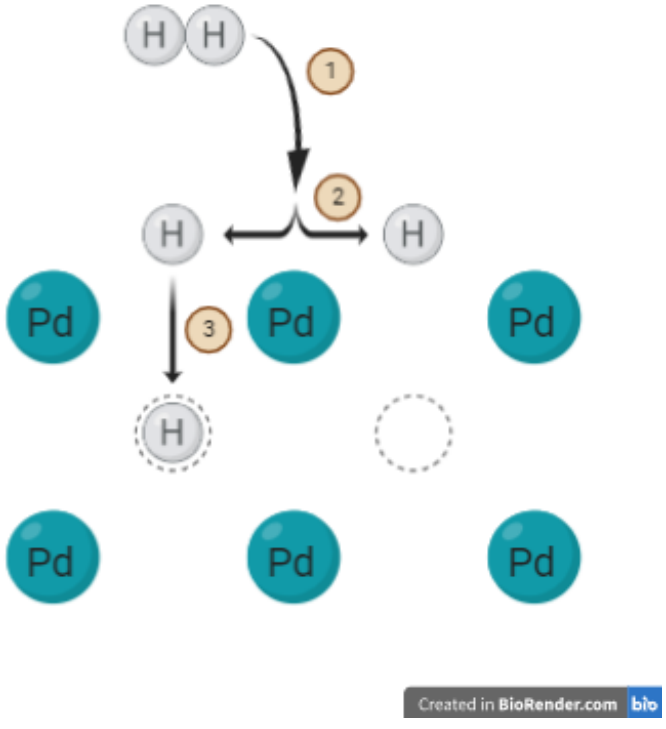


**Figure 2.2:** Palladium hydride formation. Molecular hydrogen incident on the palladium surface are dissociated into atomic hydrogen, with the metal acting as a catalyst. The atomic hydrogen diffuse into the lattice and occupies the interstitial sites.

For low hydrogen pressures, the concentration of atomic hydrogen inside the metal

lattice will be small, and the hydrogen atoms scarcely distributed. This material, a solid solution of hydrogen inside a metal, is called an $\alpha$-phase metal hydride.[14] As the hydrogen pressure increases, so does the concentration of hydrogen in the lattice, and ultimately, for temperatures below a certain critical temperature $T_c$, areas will form where hydrogen atoms occupy interstitial sites adjacent to each other. Such a phase is called a $\beta$-phase metal hydride, and at a certain hydrogen pressure the two phases will coexist.[14] Figure 2.3 illustrates the two metal hydride phases, as well as the coexistence region, denoted here as the $\alpha + \beta$-phase.

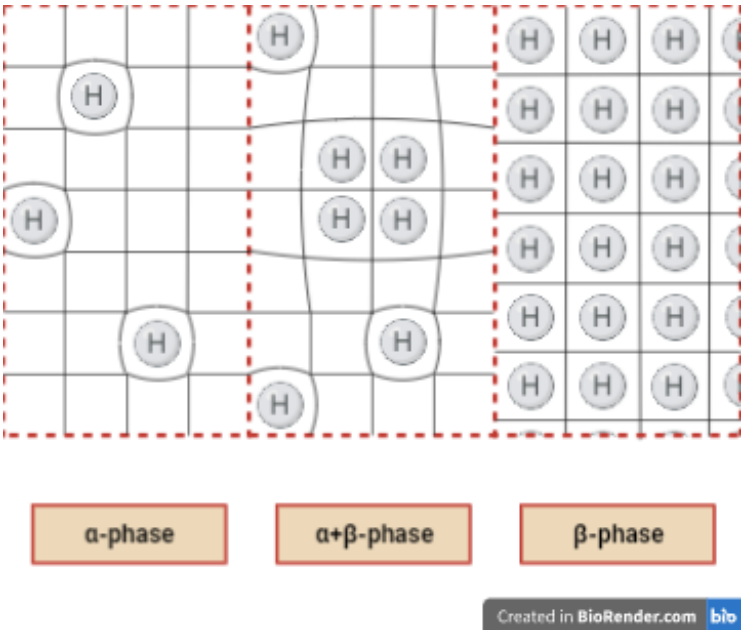


**Figure 2.3:** An illustration of an $\alpha$-phase (low hydrogen pressures) is shown in the left column. Similarly, the coexistence region (plateau pressure) consisting of both $\alpha$- and $\beta$-phases, and the pure $\beta$-phase (high hydrogen pressures), are shown in the middle and right columns, respectively.

Important to highlight is the lattice expansion that occur during the hydride formation, which results in a larger lattice constant in the metal hydride compared to the pure metal. This is of importance for hydrogen detection as the particle volume influences its LSPR response.

At the coexistence region, for isotherms below the critical temperature, the H/Pd ratio increases while the hydrogen pressure remains constant, until large domains of $\beta$-phase forms and pressure increases again. This results in pressure plateaus in the phase diagram at the coexistence region, and can be seen in figure 2.4a).

### 2.2.2 Hysteresis

When hydrogen is being absorbed in the metal, the lattice becomes strained as seen in figure 2.3. At the coexistence region, during transition between $\alpha$- and $\beta$-phases, the energy barrier that has to be overcome in order for the transition to occur, is different for hydride formation and decomposition. This means that the transition

pressure (plateau pressure) will depend on the direction of the phase transition, or in other words, if a $\beta$-phase hydride is formed or decomposed.[16] This behaviour is called hysteresis and becomes important in hydrogen sensing since the signal from such a device would inevitably include a dependence of the hydrogen pressure history, complicating the readout immensely.[17]

By pre-straining the metal lattice, it is possible to reduce and even eliminate the hysteresis effect in metal hydrides at ambient temperatures. This is done by alloying, using a metal with a larger lattice constant. In the case of palladium, alloying with 25% gold has been demonstrated to almost completely remove the hysteresis.[17] Figure 2.4 shows an illustration of typical pressure-composition isotherms of a hydride forming metal. In a), a material with a large amount of hysteresis is depicted, while b) shows a material where the hysteresis have been suppressed almost completely, for example by alloying. Note how the alloying not only decreases the pressure gap, but also introduces a slope at the coexistence region.

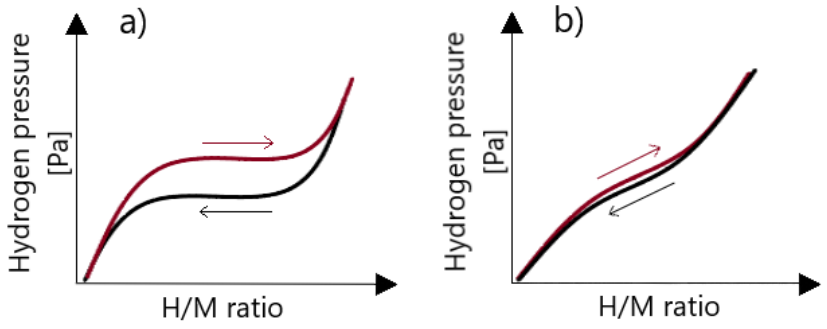


**Figure 2.4:** Pressure-composition isotherms of materials exhibiting a) hysteresis, b) suppressed hysteresis. Red arrows correspond to $\beta$-phase formation and black arrows to $\beta$-phase decomposition.

### 2.2.3 Metal-Hydride LSPR Hydrogen Sensing

Although a complex phenomenon, LSPR enables hydrogen sensing based on a very simple effect. The hydride formation shifts the plasmon peak towards the red part of the spectrum, broadens the peak and decreases its height. What this leads to, is the possibility to measure among other things, the spectral change in LSPR peak position ($\Delta\lambda_{LSPR}$), or the change in extinction at the peak ($\Delta\text{Ext}_{peak}$), as shown in figure 2.5. These signals can be used as a read-out for the hydrogen concentration in the hydride, which in turn stand in direct correlation to the hydrogen partial pressure in the surrounding.

Another read-out from the plasmon peak shift is the change in extinction at a single wavelength ($\Delta$Ext). This is a neat feature in a miniaturized, low cost setup where the use of narrow range LEDs are preferred over a white light source. As a consequence, this signal is of special importance for this thesis and is directly related to the read-out procedure used when working with the miniaturized device.

The LEDs should then be chosen in such a way that it matches the wavelength where ΔExt is maximized. Figure 2.5 demonstrates this optimization problem quite clearly. In the spectral range between the two peaks there is an area, marked in blue, where ΔExt is very low, or even zero. Hence, this spectral range should be avoided when choosing single wavelength LEDs. Finding the right LED, to maximize the signal from the sensor device, will be an important part of this thesis and the process towards a commercially attractive product.

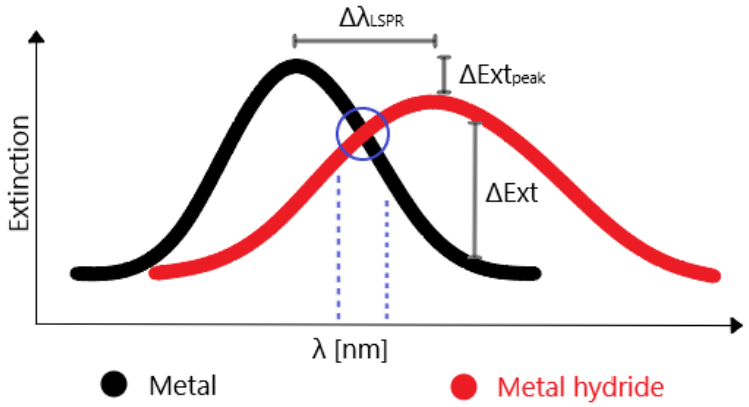


**Figure 2.5:** Plasmon peaks of a metal (black) and its related metal hydride (red), illustrating the peak shift caused by hydride formation. The read-out signals $\Delta\lambda_{LSPR}$, $\Delta\text{Ext}_{peak}$ and ΔExt are indicated by gray bars. The spectral region marked in blue highlights low-signal sensing region when using the ΔExt read-out.

## 2.3 Hydrogen Sensing in the LUFT-device

While the read-out signal in the reactor setup simply consists of the absolute change in extinction at a chosen wavelength, the read-out from the LUFT-device is approached in a slightly different way. The device uses a setup of two LEDs, of which one is used as a reference channel, adjusted by feed-back loops in order to compensate for temperature fluctuations. The read-out in the end, is a relative change in the transmitted light detected by the photodiode, compared to the reference signal. This relative signal is expressed in the unit [mil], meaning parts per thousand. A signal equal to 20 [mil] hence corresponds to a 2% change in the total transmission. To be able to compare experiments done in the LUFT-device with reactor measurements, the absolute extinction change obtained in the reactor should be converted into relative transmission change (in [mil]) according to equation 2.12.

$$\text{Relative transmission change [mil]} = \frac{\text{Absolute extinction change}}{1 - \text{Extinction at 0\% } H_2} \times 1000 \quad (2.12)$$

# 3
# Methods

In this chapter, experimental procedures and methods used for sensor fabrication, LSPR response simulations and data analysis are presented.

## 3.1 Simulations

Simulations of the LSPR response of oblate spheroids were performed in Matlab, using the equations described in section 2.1.2. For the dielectric functions of different PdAu-alloys, data was obtained from the research group led by Paul Erhart. The data was calculated from time-dependent density functional theory (TDDFT). It does not yet exist in the literature, but is publicly available at the research groups webpage.[18] In the same way as done by Langhammer et al., an effective refractive index of 1.26 was used for the surrounding medium, corresponding to the average of air (n=1) and the glass substrate (n=1.52).[11]

As a simplified way of simulating hydrogen presence, the LSPR response due to hydride formation was approximated by a change in the surrounding refractive index. First, the peak shift (26 nm) caused by a 4% hydrogen concentration for a 210x25 nm, $Pd_{80}Au_{20}$ nanodisc was observed experimentally. In the simulation software, an updated refractive index corresponding to the same peak shift was determined. Then, it was assumed that this new refractive index (1.32) represents the real peak shift occuring due to the volume expansion and altered dielectric function of the nanoparticles, caused by the hydride formation. By comparing the plasmon peaks for the two different refractive indices, the idea was to get a picture of at which wavelength the change in extinction cross-section $\Delta\sigma_{Ext}$ was maximized. Similar simulations were then repeated for different sizes and aspect ratios of the nanoparticles in order to determine optimal nanoparticle size properties for hydrogen sensing.

## 3.2 Experimental

### 3.2.1 Sensor Chip Manufacturing

The sensor chips used in the experiments were manufactured by hole-mask colloidal lithography[19] (HCL) in a cleanroom environment at Chalmers University. The fabrication followed the procedure of Nugroho et al.[20]. First, a cleaning process using ultrasonic agitation in acetone, isopropyl alcohol (IPA), and deionized (DI) water was performed on the glass substrates. Then, the wafers were spin-coated with

a thin layer of poly(methyl methacrylate) (PMMA), applied using a rotation speed of 2000 rpm for 1 minute, after which a soft baking was performed at 443 K for 10 minutes. The hydrophilicity of the samples were then increased by oxygen plasma treatment for 5 seconds, before pipetting a solution of polydiallyldimetylammonium (PDDA) on the surface. The solution was rinsed off after 40 seconds using DI water, and left a positively charged surface layer on the PMMA. Depending on the desired nanoparticle size, a suspension containing negatively charged polystyrene (PS) beads of corresponding size (140 or 210 nm) was applied to the surface. The suspension was rinsed off by DI water after 3 minutes, samples were blown dry using nitrogen, leaving a dispersed array of polystyrene beads on the surface. During the next step, chromium (Cr) was evaporated onto the samples, until a 15 nm thick film was formed. Tape stripping was used in order to remove the PS beads, leaving holes in the Cr film were the beads had been positioned. A 5 minute treatment with oxygen plasma then etched away the PMMA layer below the holes before palladium and gold were deposited through the mask, in sequence. Finally, the mask was removed by dissolving the PMMA layer in acetone, and the final nanodisc-covered substrates were annealed in a flow furnace at 773 K for 12 or 24 hours, in order to obtain a homogeneous alloying.

The fabrication of sensor chips to be used in the LUFT-device contained further steps, as it included the addition of a microheater. The mask for the heaters were produced using e-beam lithography. The microheater pattern was then transferred from the mask to the wafer by photolithography. The final steps of the fabrication included e-beam evaporation of platinum onto the wafer, followed by a lift-off process removing the evaporation mask.

### 3.2.2 Measurements in the Chalmers Reactor Setup

The experiments done with the Chalmers reactor was performed for two main reasons; to evaluate the optimal sensing wavelength for monochromatic sensing in the LUFT-device, and to act as a benchmark for such upcoming measurements.

The reactor setup consisted of a custom-built *Insplorion X1* instrument. A schematic can be seen in figure 3.1. The reactor is made up by a quartz reactor tube, in which heat coils are included for temperature control. The sensor chips was mounted onto the sensor holder, and was then slid into the reactor chamber, whose gas inlet was connected to three different mass-flow controllers (MFCs). To achieve the wanted hydrogen concentrations, each MFC regulated the flow of one of the following gas lines:

- Pure argon gas
- Argon gas with 4% hydrogen
- Argon gas with 25% hydrogen

Hydrogen concentrations in the range from 50 ppm to 4% were investigated, using a flow-rate of 550 ml/min. For each concentration, three cycles were repeated after each other, with desorption periods separating them (pure argon gas).

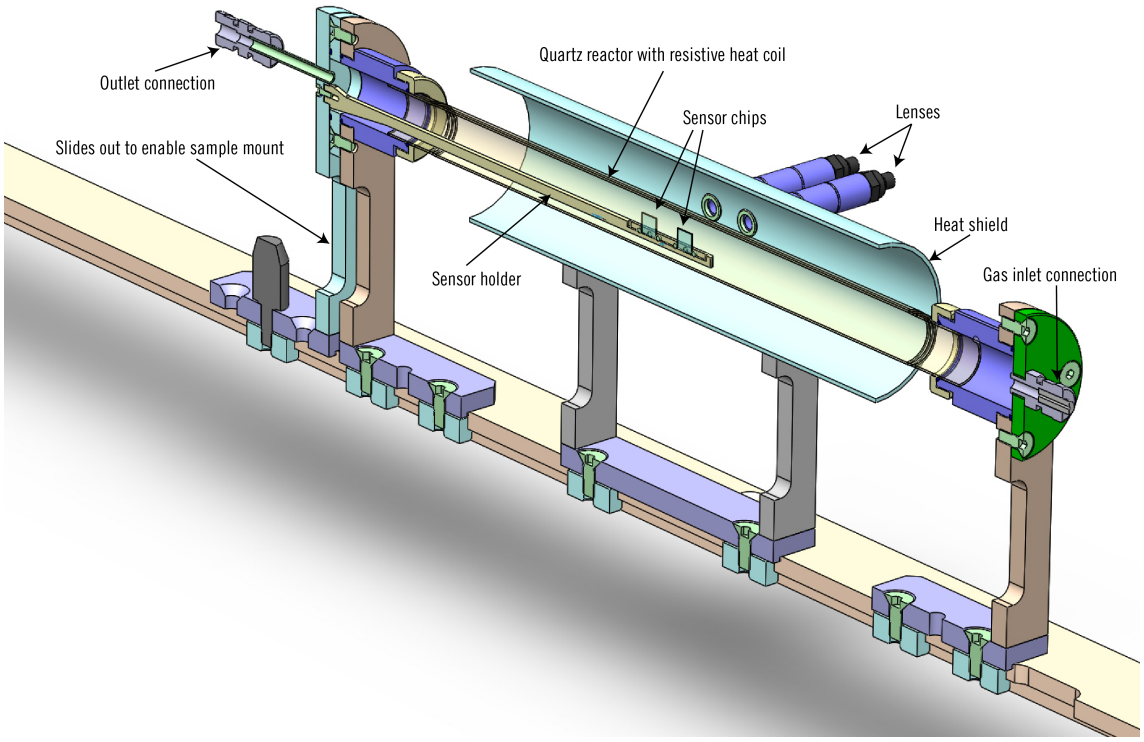


**Figure 3.1:** Schematic of the *Insplorion X1* instrument. Gas enters through the gas inlet connection seen to the right. It is transported passed the sensor chips and exits through the outlet connection to the left. The collimating lenses allowed fiber optic connections to and from the light source and detector.

The instrument used a white light source in the form of a tungsten halogen lamp, and a spectrometer detector, both connected via fiber optics, for LSPR read-out. Collimating lenses was used in order to achieve parallel light passing through the sensor. All measurement settings as well as read-out data collection was done using the associated *Insplorer* software. Measurements were performed on sensor chips containing nanoparticle arrays for several different sizes, within the range of 140-210 nm. Common for all sensors was the nanoparticle height of 25 nm.

### 3.2.3 Measurements in the LUFT-device

Initially, three experiments was performed using a modified version of the existing LUFT-device, designed for $NO_x$ detection. This was done by placing a sensor chip with 210x25 nm $Pd_{80}Au_{20}$ particles inside the device. For protection of the technology involved, no accurate schematic can be shown here, however, a very simplified version are displayed in figure 3.2. The gas inlet was connected to the same three MFC's used for the reactor but with a flow-rate of 300 ml/min. The desired flows of argon, 4% $H_2$ in argon and 25% $H_2$ in argon was again specified using the *Insplorer* software. Concentrations from 0.01%-4% hydrogen was evaluated in the LUFT-device.

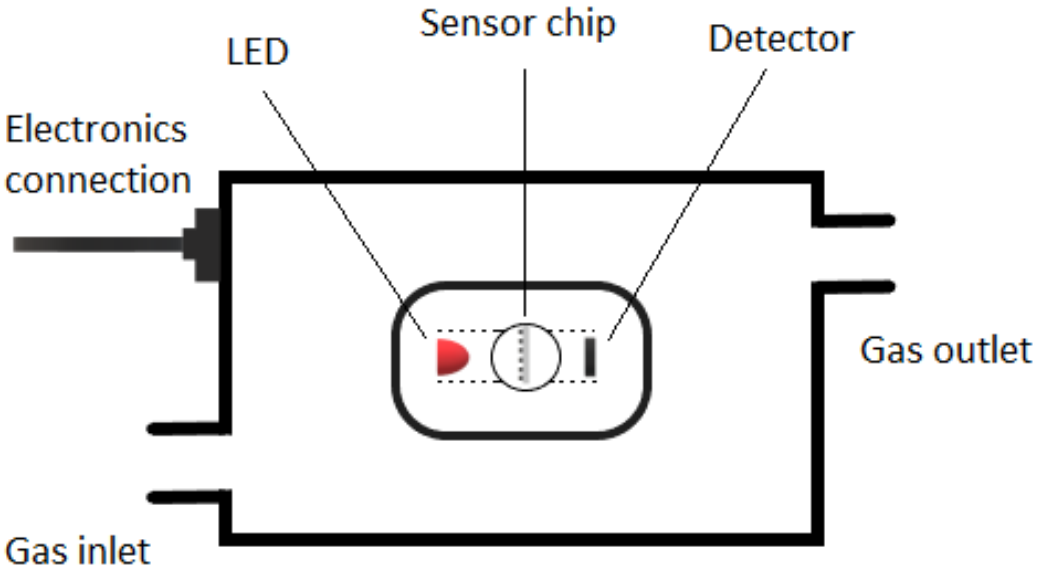


**Figure 3.2:** Schematic of the LUFT-device. Gas enters at the inlet to the left, then passes through the empty volume until it reaches the sensing area around the sensor chip. The photodiode detector registers the change in transmission of light as hydride formation takes place in the nanoparticles on the sensor chip.

Inside, the device contains a chip, on which the sensing equipment is mounted. In the schematic, this is shown as the rectangle with rounded corners. The sensing equipment consists of an LED (in reality there are actually two, as one extra is needed as a reference signal), the sensor chip and a photodiode detector. A cylinder-shaped channel connects the LED and the detector, indicated by the dashed lines. The sensor chip needs to be mounted in such a way that the light from the LED passes through it on its way to the detector. The rest of the device is just an empty volume. The initial setup used an LED light source centered around 940 nm. The photodiode detector possessed a response curve that can be seen in figure 3.3. The detector is optimized for wavelengths around 850 nm, but exhibits at least half of the peak response for wavelengths in the range between 600-1000 nm.

All three measurements were then used to construct a calibration curve for this specific device configuration. Succeeding measurements were performed in a similar manner, first with the 940 nm LEDs replaced with LEDs centered around 650 nm, and then a fourth measurement using the 940 nm LEDs was repeated, this time with an improved sensor mounting. The reason for evaluating a device setup using 650 nm LEDs was that the access to 715 nm LEDs fell short, and 650 nm was the closest available wavelength that could be attained in time.

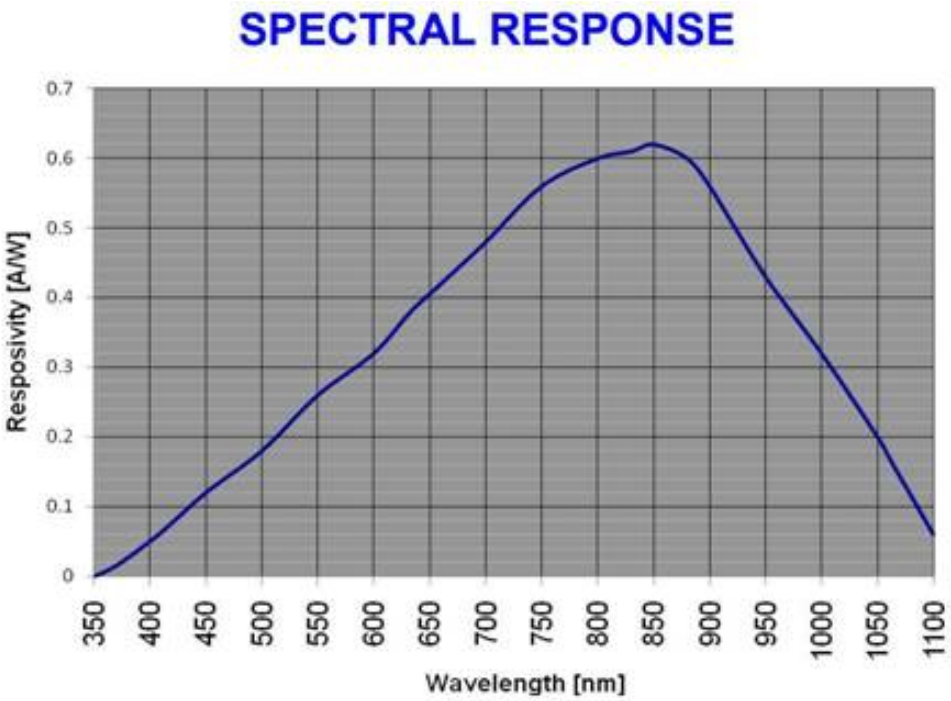


**Figure 3.3:** Response curve of the photodiode detector.

## 3.3 Plotting and Data Analysis

All data plotting and analysis was performed in Matlab, using self-built scripts, with one exception. When extracting the magnitudes of the extinction or transmission changes from the experimental data, a function from the research group at Chalmers was used. All codes are found in Appendix A.1. When statistic parameters such as mean values and standard deviations were needed, the built-in Matlab functions (mean(X) and std(X)) were used for the extraction of these.

# 4

# Results & Discussion

This chapter presents the main findings and most important results of the project. It also includes brief discussions on the findings, their validity and on possible improvements. The results are mainly presented in a chronological order, as this more clearly reflects the working process of this thesis. Therefore, the simulations that were performed are presented first, followed by experimental results from the reactor, and then from the LUFT-device.

## 4.1 Simulations

### 4.1.1 Optimal Wavelength for Hydrogen Sensing

The simulated optical response caused by an increase of the hydrogen pressure from 0% to 4% can be seen as the blue plots in figure 4.1. More specifically, what is plotted in blue are the simulated extinction cross-sections of 210x25 nm $Pd_{80}Au_{20}$ particles, for the two different concentrations. Included as a comparison (shown in red), are the real experimental spectras of the same particles, from the Chalmers reactor setup.

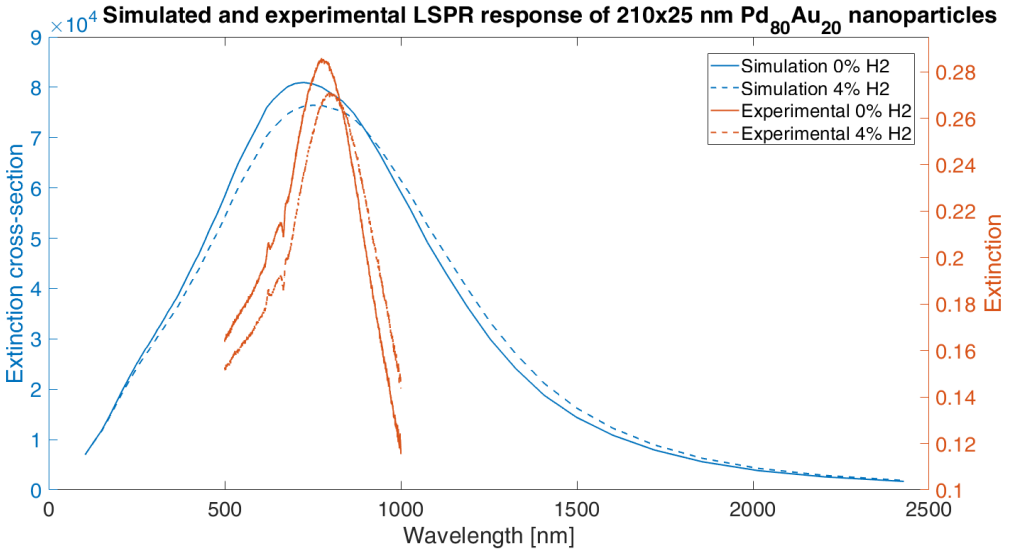


**Figure 4.1:** Extinction cross sections (simulation) and extinction (experimental) as a function of wavelength, for two different hydrogen concentrations, 0% (solid) and 4% (dashed).

The comparison shows that the model underestimates the experimental peaks by approximately 50 nm. When it comes to the width of the peaks, the model by far overestimates the real values. This stands in contrast with the results obtained by Langhammer et al.[11], who found excellent agreement between simulation and experiments, for both peak positions and line width of the peak. To exclude the possibility that the discrepancies between simulation and experimental results were caused by error(s) in the Matlab programme, calculations were performed on pure Pd particles in the size range of 100-300 nm, which were subsequently compared to the results of Langhammer et al. [11]. These simulations showed good agreement with their results regarding the line width (FWHM) of the peaks, as well as peak positions and extinction cross-sections of the nanoparticles. As a consequence, the discrepancies were not caused by computational errors. What could instead be the reason, is the fact that the nanoparticle arrays used in this thesis, obtained from HCL fabrication, are not periodically ordered, but rather possess an amorphous structure, with both short range order, and random distribution of particles at longer distances. It has been shown, by Antosiewics et al. [21], that amorphous arrays of plasmonic nanoparticles exhibit oscillatory optical responses that depends strongly on the particle-particle separation, and in particular in the case of line width. Therefor, the model used here, while correct for simulating single nanoparticle LSPR response, is simply not suitable for simulating an amorphous matrix of nanoparticles.

The low ability to describe the peak widths and peak positions does ultimately affect with what accuracy the model can estimate the optimal as well as non-optimal sensing wavelengths of the device. In figure 4.2, the simulated and experimentally obtained signals are plotted. The signals shown are the difference of the 0% and 4% spectra of figure 4.1, for both the simulation and experimental scenario.

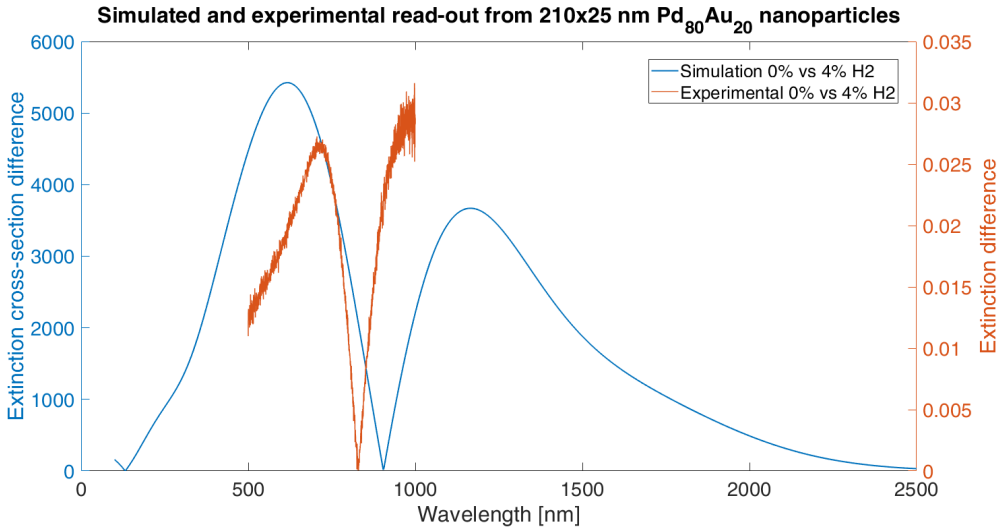


**Figure 4.2:** $\Delta$Ext (experimental) and $\Delta\sigma_{ext}$ (simulation) due to an increase in hydrogen concentration from 0% to 4%. Optimum and non-optimum sensing regions are observed in both curves, with spectral offsets between simulation and experimental results.

Both curves feature a distinct minima, where the achieved signal has its lowest point, hence corresponding to the non-optimal sensing spectral region. The offset between the simulation and experimental values are 74 nm, with the real values at 830 nm compared to 904 nm in the simulation. The model predicts the left optima to have higher signal than the right one, unlike the experimental values. It also underestimates the spectral position of the left optima and overestimates the position of the right optima. It can not be excluded that the very much simplified approach of simulating hydride formation introduced here, could have given reasonable predictions of the corresponding plasmonic responses. However, in order to evaluate this, the amorphous structure of the nanoparticle arrays need to be considered in the underlying model.

## 4.2 Experiments at the Chalmers Reactor

### 4.2.1 Optimal Wavelength for Hydrogen Sensing

In figure 4.3, ΔExt have been calculated by subtraction of two different extinction spectra, belonging to 210x25nm $Pd_{80}Au_{20}$ nanodiscs, in pure argon gas and argon gas mixed with 4% hydrogen, respectively.

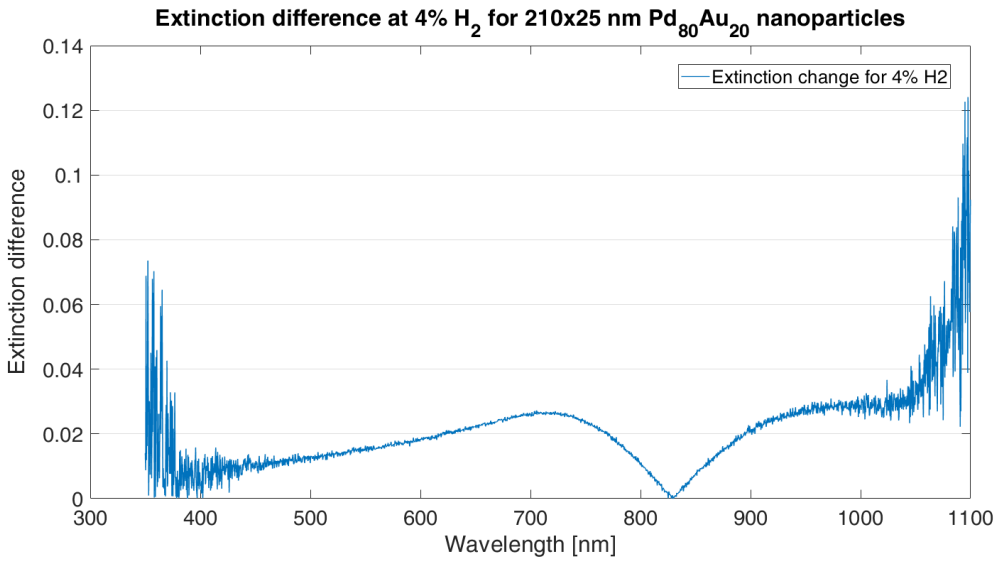


**Figure 4.3:** ΔExt for 4% hydrogen, highlighting the two optimum sensing regions around 715 nm and 940 nm (maxima), alongside the non-optimal sensing region centered around 830 nm (minima).

The region with the lowest signal can be seen clearly between 800-850 nm, with a minimum at 830 nm. For wavelenghts shorter than 450 nm and longer than 1000 nm respectively, the signal is characterized by high noise. This is due to the grating dispersing the light not being effective at such long wavelengths. However, in the stable region, between 500-1000nm, the signal exhibits two maxima, one around 710-730nm and one in the plateau-like range from 940-1000nm. Hence, the hydrogen sensing should preferably be performed at one of these wavelengths. It should be

stated that this evaluation only was performed for 4% hydrogen, and that the optimum wavelength may vary with hydrogen pressure. Such an analysis has however already been performed by Wadell et al.[17], where hydrogen pressures in the range from 1-1000 mbar were investigated. Their results implies optimum wavelengths on each side of the plasmon peak, supporting the outcome of the single-concentration evaluation performed here.

Regarding which wavelength to prefer, it can be seen in figure 4.3 that ΔExt is slightly higher at the 940 nm peak, compared to the one at 715 nm, but it also exhibits more noise, again because of the inefficient grating. The overall signal (Ext), is also lower at the longer wavelength, as seen below in figure 4.4 . This could be another source of the higher noise seen at these wavelengths. As a higher noise could affect the accuracy of the sensing, both wavelengths should be evaluated.

### 4.2.2 Achievable Extinction Change

Figure 4.4 shows the extinction changes achieved in the Chalmers reactor setup for a 210x25 nm $Pd_{80}Au_{20}$ sensor chip, for different hydrogen concentrations and measured at the two previously discussed wavelengths, 715 nm and 940 nm, respectively.

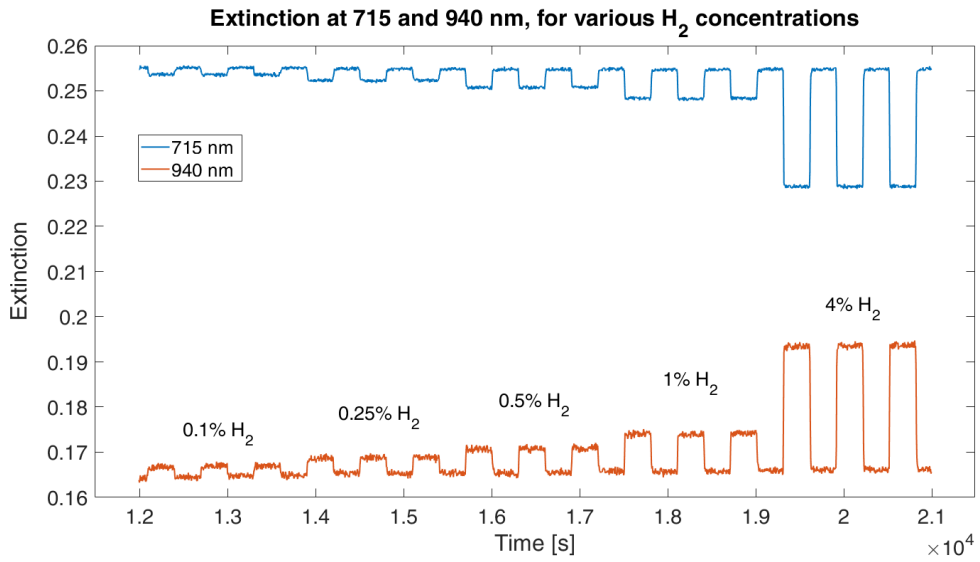


**Figure 4.4:** Extinction caused by an array of 210x25 nm $Pd_{80}Au_{20}$ nanoparticles on a glass substrate, measured at two different wavelengths, for different hydrogen concentrations in argon.

To more clearly see the difference, the extinction changes from figure 4.4 are summarized in table 4.1. The values shown are mean values of the three cycles performed for every concentration. The 0.25% concentration has been excluded as it was not used in the LUFT-device experiments.

| Conc. [%] | Extinction change @715 nm | Extinction change @940 nm |
|---|---|---|
| 4 | 0.0266 | 0.0286 |
| 1 | 0.0068 | 0.0095 |
| 0.5 | 0.0046 | 0.0065 |
| 0.1 | 0.0021 | 0.0034 |

**Table 4.1:** Absolute extinction change for a range of $H_2$ concentrations, measured at 715 nm and 940 nm wavelengths, using the Chalmers reactor setup.

What becomes evident from these results are that ΔExt are larger at 940 nm compared to 715 nm. This is true not only for 4% hydrogen, but also for the lower concentrations. In fact, the difference between the two are even larger for lower concentrations. At 0.1% hydrogen, ΔExt are 62% higher at 940 nm, while for 4% hydrogen, the difference is merely 7.5%.

In order to compare these results with read-outs from the LUFT-device, the absolute extinction changes need to be recalculated into relative transmission changes, according to equation 2.12. Figure 4.5 shows the relative transmission changes for the reactor experiments displayed in figure 4.4, but it also includes results measured at 650 nm.

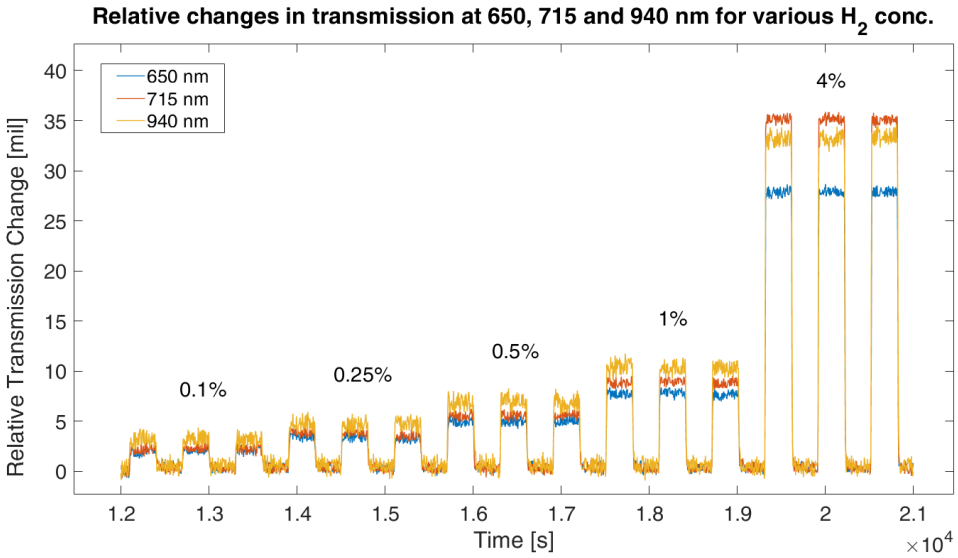


**Figure 4.5:** Relative transmission changes from reactor measurements, caused by an array of 210x25 nm $Pd_{80}Au_{20}$ nanoparticles on a glass substrate, measured at three different wavelengths, for different hydrogen concentrations in argon.

The mean values from figure 4.5 are shown in table 4.2, where the relative transmission changes are denoted as $\Delta Trans_{rel}$.

| Conc. [%] | $\Delta Trans_{rel}$@650 nm [mil] | $\Delta Trans_{rel}$@715 nm [mil] | $\Delta Trans_{rel}$@940 nm [mil] |
|---|---|---|---|
| 4 | 28.32 | 35.38 | 34.09 |
| 1 | 8.18 | 9.32 | 11.11 |
| 0.5 | 5.29 | 6.06 | 7.81 |
| 0.1 | 2.72 | 2.77 | 4.04 |

**Table 4.2:** Relative transmission change for a range of $H_2$ concentrations, measured at 650, 715 and 940 nm wavelengths using the Chalmers reactor setup.

Using this read-out, the highest signals are achieved at 940 nm for concentrations below or equal to 1%, and at 715 nm for 4%. Hence, these results suggest that the longer wavelength should be used if the aim is to detect low concentrations of hydrogen (1% or lower), while a shorter wavelength (715 nm) are to be preferred at concentrations of 4% and higher. Note that this is only the case when the read-out is in the form of relative transmission change, and not if the measured entity is absolute extinction. From a safety sensor application perspective, the concentration range of interest are mainly that below the flammability limit of hydrogen, at 4%, which speaks in the favour of the longer wavelength LED.

### 4.2.3 Response Time Evaluation

The mean response times ($t_{90}$) for each hydrogen concentration, calculated from the experiment in figure 4.4, are highlighted in table 4.3. As can be seen, the response time until 90% of the full signal is reached, does not vary for the higher concentrations evaluated (0.5-4%), sitting at 10 seconds for all of them. The lowest concentration shows a slower response time of 20 seconds.

| Conc. [%] | $t_{90}$ [s] |
|---|---|
| 4 | 10 |
| 1 | 10 |
| 0.5 | 10 |
| 0.1 | 20 |

**Table 4.3:** Response times from experiments in the Chalmers reactor setup.

That the response times does not vary between 0.5-4% is because what is actually measured is the time it takes for the gas volume inside the reactor tube to be exchanged for gas with another hydrogen concentration, i.e. the time constant of the system. The response time of the hydride formation is considerably faster, as shown by Nugroho et al.[6]. The response times from these experiments are not of any particular interest in this thesis except as a benchmark when comparing with the measurements performed with the LUFT-device, which will be discussed in a later section.

## 4.3 Experiments with the LUFT-device

### 4.3.1 940 nm LEDs

A typical measurement done using the 940 nm LED, with a randomized order of hydrogen concentrations, is shown in figure 4.6. Distinct peaks can be seen for hydrogen concentrations of 0.1% and above.

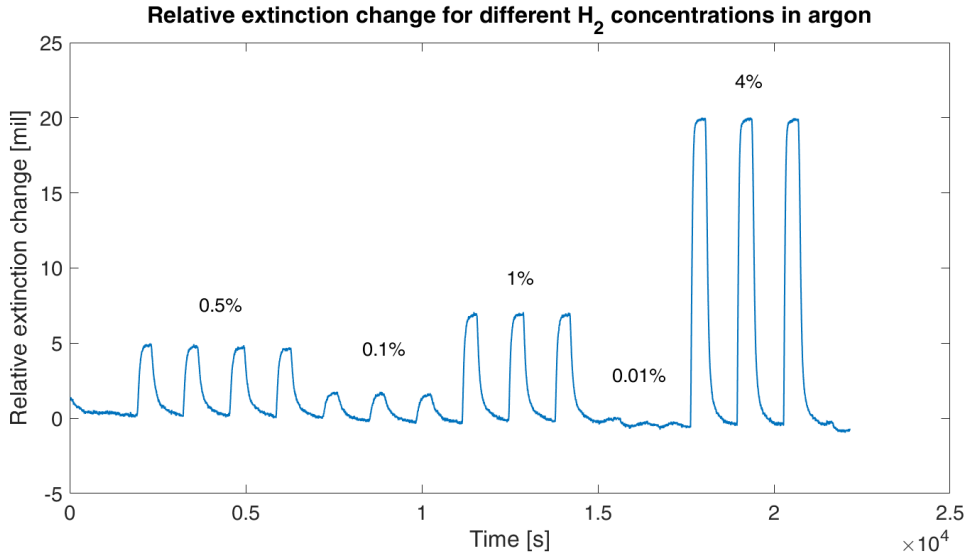


**Figure 4.6:** Relative extinction change from measurements in the LUFT-device, using 940 nm LEDs as light source, for hydrogen concentrations in the range of 0.01% to 4%.

Visually, these results quite closely resembles the ones from the reactor experiments. There are, however, some important differences that becomes apparent when looking closer at the response curve. First of all, the relative change in extinction compared to the ones obtained in the reactor, are considerably smaller, as seen from table 4.4.

| $H_2$ conc [%] | Signal [mil] | Standard deviation [mil] |
|---|---|---|
| 4 | 20.26 | 0.14 |
| 1 | 7.03 | 0.11 |
| 0.5 | 4.49 | 0.12 |
| 0.1 | 1.75 | 0.15 |
| 0.01 | 0.32 | 0.05 |

**Table 4.4:** Mean relative transmission changes and their standard deviations in the LUFT-device, using 940 nm LEDs.

For 4% hydrogen, the read-out signal in the LUFT-device is only 59.43% of the one obtained in the reactor setup. The numbers for 1%, 0.5% and 0.1% are 63.27%, 57.49% and 43.31%, respectively. After the three experiments were performed with

the LUFT-device, using the 940 nm LED's, it was found that the mounting of the sensor within the device had been slightly misaligned with the light path. This ultimately resulted in that more leak-light found its way from the LED to the photodiode detector without passing through the sensor chip. How much this decreased the signal is hard to tell, but in order to determine this, another experiment was performed with a correct mounting. The result is summarized in table 4.5

| $H_2$ conc [%] | Signal [mil] | Standard deviation [mil] |
|---|---|---|
| 4 | 25.60 | 0.31 |
| 1 | 10.20 | 0.14 |
| 0.5 | 6.19 | 0.07 |
| 0.1 | 2.26 | 0.11 |
| 0.01 | 0.28 | 0.06 |

**Table 4.5:** Mean relative transmission changes and their standard deviations in the LUFT-device, using 940 nm LEDs with improved mounting of the sensor chip.

The signal obtained in the device using this sensor mounting was increased for all concentrations except for the lowest one (0.01%). Now, the read-outs for 4%, 1%, 0.5% and 0.1% hydrogen reaches 75.10%, 91.81%, 79.26% and 81.59% of the signal in the reactor, respectively. A hypothetical reason for the remaining difference in signal could be leakage of gas from the device, and that the concentrations of hydrogen surrounding the nanoparticles simply does not reach the concentration levels of the inlet gas stream. As the case is today, the sensor is kept inside a box, with a volume much larger than the volume where the actual sensing takes place. Therefor there is a chance that some amount of hydrogen, with its high volatility, escapes the volume without being detected. In other words, the equilibrium hydrogen concentration reached after replacing all the gas of a previous concentration, might be a bit lower than the inlet concentration, leading to a lower signal. Another reason could be that the LED has a certain wavelength bandwidth, and that the signal in the LUFT-device therefore corresponds to the signal from all the wavelengths of this bandwidth, while in the reactor setup, the signal can be accurately measured at a specific wavelength. What can be concluded from these results is that given the well defined inlet concentrations, this setup of the LUFT-device achieved the read-out signals of table 4.5.

The second difference of the LUFT response curve compared to the reactor measurements, are the $t_{90}$ response times, which are much longer in the LUFT-device.

| Conc. [%] | $t_{90}$ [s] |
|---|---|
| 4 | 80 |
| 1 | 120 |
| 0.5 | 130 |
| 0.1 | 160 |
| 0.01 | 245 |

**Table 4.6:** Response times ($t_{90}$), from measurements done in the LUFT-device, for a range of hydrogen concentrations in argon gas.

A probable reason for these longer response times, shown in table 4.6, again lies within the large empty volume of the device. Even if the box was to be considered completely leak-proof, the time it would take to replace its content with gas of another hydrogen concentration, would be much higher than in the reactor setup. It should be mentioned that the flow rate used in the reactor was higher (550 ml/min) compared to the LUFT-device (300 ml/min). Despite this, there is still reason to believe that the kinetics could be improved by decreasing the volume inside the device to more closely match the sensing volume of the sensor chip.

### 4.3.2 650 nm LEDs

The experimental result from the single experiment done with 650 nm LEDs is displayed in figure 4.7. Responses are generally higher compared to the initial measurements using 940 nm LEDs mounted incorrectly.

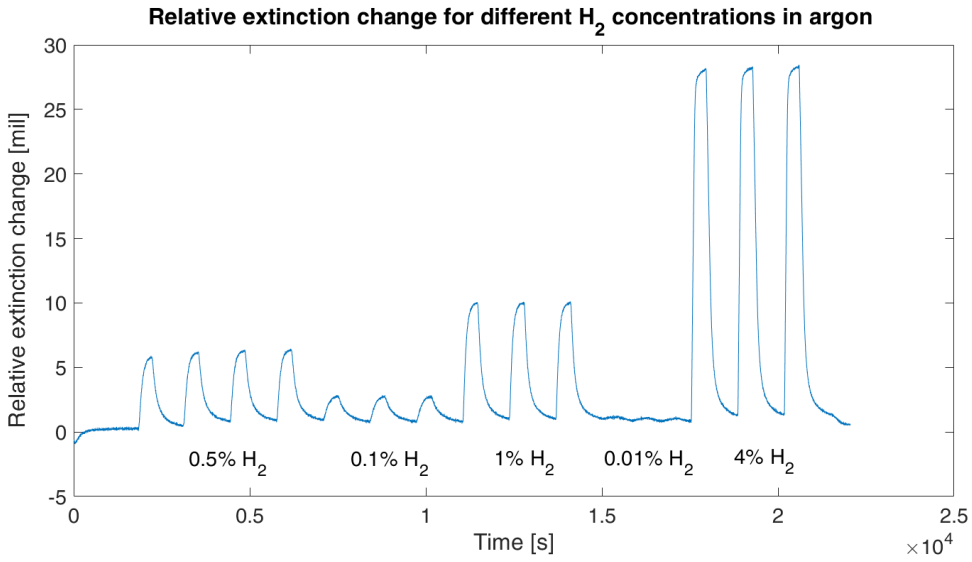


**Figure 4.7:** Relative transmission changes from measurements in the LUFT-device, using 650 nm LEDs as light source, for hydrogen concentrations in the range between 0.01% to 4%.

The means of the transmission changes from figure 4.7 are listed in table 4.7. For this LED wavelength, the signal from 4% hydrogen is 95.41% of the reactor signal, a

result that should be considered as very good. What is even more remarkable is that for the concentrations 0.5% and 1%, the relative signal is higher in the LUFT-device compared with the reactor, a very unexpected result.

| $H_2$ conc [%] | Signal [mil] | Standard deviation [mil] |
|---|---|---|
| 4 | 27.02 | 0.24 |
| 1 | 9.08 | 0.12 |
| 0.5 | 5.57 | 0.12 |
| 0.1 | 1.99 | 0.07 |
| 0.01 | 0.30 | 0.05 |

**Table 4.7:** Mean relative transmission changes and their standard deviations, using 650 nm LEDs

Unless this depends on some measurement error or that the LEDs have a longer wavelength than stated, the only explanation that could be thought of is the fact that 650 nm is situated, spectrally, on the left flank of the left sensing optimum, as displayed in figure 4.3 in a previous section. Since the LEDs are not perfectly monochromatic, but rather possess a certain bandwidth, the photons with wavelengths longer than 650 nm will result in a slightly higher signal compared to those with a shorter wavelength. If this distribution is not balanced perfectly around 650 nm, or if the difference in the response between for example 655 and 650 nm is larger than for 645 and 650 nm, such a component-dependent cause could influence the signal from the LUFT-device.

### 4.3.3 Calibration Curves for the LUFT-device

As a final note on the measurements done in the LUFT-device, it can be said that when detecting lower concentrations of hydrogen ($\leq 1\%$), the 940 nm LEDs gives the highest signals, as predicted by reactor measurements. This is clearly displayed in the calibration curves found below in figure 4.8.

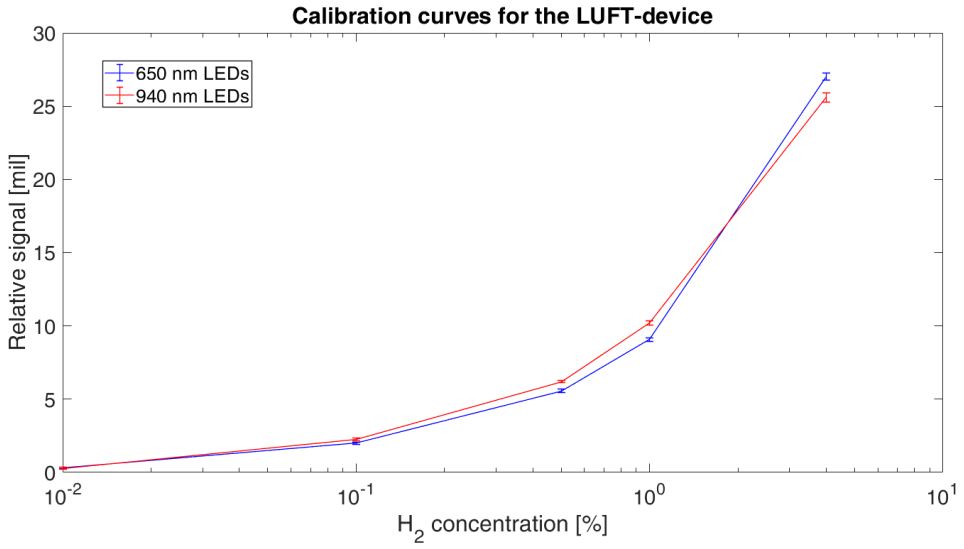


**Figure 4.8:** Calibration curve of the LUFT-device equipped with 650 nm and 940 nm LEDs. Shown is the relative transmission changes, plotted versus hydrogen concentration (%), on a log scale.

The only exception to this rule is the lowest signal measured (0.01%), however, for that concentration, the hydride formation did not reach saturation, and no conclusions can really be drawn. When the goal is to sense high concentrations of hydrogen (4% and higher), the best result is achieved with 650 nm LEDs.

Recalling the target requirements stated in section 1.2, this thesis has demonstrated a first attempt to miniaturize the nanoplasmonic hydrogen sensing, that successfully meet the requirements on detection range and accuracy, falling short only on the response time, out of the requirements investigated. This may also possibly be the hardest requirement to meet in a device not employing a vacuum system. As previously stated however, it is believed that the kinetics of the LUFT-device could be enhanced considerably, and it remains to be seen how fast it will become in the future.

# 5
# Conclusion

As concluding remarks this thesis has demonstrated that miniaturized single-wavelength hydrogen sensing is possible by simply integrating the sensing technology from Chalmers onto the NPS-platform developed by Insplorion. The LUFT-device meets the requirements stated by the U.S. Department of Energy regarding detection range and accuracy, but falls short on the response time requirement of <1s. The simulation of hydride formation did not meet the expectations and was therefore not used in the sensor optimization process, however it helped gain valuable knowledge and insights in the theory of LSPR.

## 5.1 Future Work

There are several aspects of this project where further investigations would be needed and were the results may be of high interest from an application perspective. For example, it would be of interest to investigate the performance of the LUFT-device when equipped with 715 nm LEDs, to see if the detection of high hydrogen concentrations could be further improved. Regarding lower concentration sensing, it would be interesting to evaluate if the performance could be enhanced by increasing the Au content in the nanoparticles. In the $Pd_{80}Au_{20}$ particles used in this thesis, there still exists some hysteresis. Increasing the Au content to around 30 at.% would be a natural next step, as it would remove all the hysteresis, and has been found to improve the sensitivity for low hydrogen concentrations.[17] Also, to add a protective coating and perform tests in more ambient-like environments will be a crucial next step, as the high selectivity is supposed to be one of the advantages of nanoplasmonic hydrogen sensors. Furthermore, the response time of the device needs to be decreased considerably in order to meet the requirements of a commercial hydrogen safety sensor. Suggested first attempts should be made either by decreasing the volume inside the device, or by building a tubing system that connects the inlet of the device and the sensing volume of the chip.

# Bibliography


[1] G. Marbán and T. Valdés-Solıs, "Towards the hydrogen economy?", International journal of hydrogen energy **32**, 1625–1637 (2007).

[2] G. W. Crabtree, M. S. Dresselhaus, and M. V. Buchanan, "The hydrogen economy", Physics today **57**, 39–44 (2004).

[3] C. Wadell, S. Syrenova, and C. Langhammer, "Plasmonic hydrogen sensing with nanostructured metal hydrides", ACS nano **8**, 11925–11940 (2014).

[4] K. L. Cashdollar, I. A. Zlochower, G. M. Green, R. A. Thomas, and M. Hertzberg, "Flammability of methane, propane, and hydrogen gases", Journal of Loss Prevention in the Process Industries **13**, 327–340 (2000).

[5] W. J. Buttner, M. B. Post, R. Burgess, and C. Rivkin, "An overview of hydrogen safety sensors and requirements", International Journal of Hydrogen Energy **36**, 2462–2470 (2011).

[6] F. A. Nugroho, I. Darmadi, L. Cusinato, A. Susarrey-Arce, H. Schreuders, L. J. Bannenberg, A. B. da Silva Fanta, S. Kadkhodazadeh, J. B. Wagner, T. J. Antosiewicz, et al., "Metal–polymer hybrid nanomaterials for plasmonic ultrafast hydrogen detection", Nature materials **18**, 489–495 (2019).

[7] K. M. Mayer and J. H. Hafner, "Localized surface plasmon resonance sensors", Chemical reviews **111**, 3828–3857 (2011).

[8] G. Grosso and G. P. Parravicini, "Chapter 7 - excitons, plasmons, and dielectric screening in crystals", in *Solid state physics (second edition)*, edited by G. Grosso and G. P. Parravicini, Second Edition (Academic Press, Amsterdam, 2014), pp. 287–331.

[9] O. Saison, G. Lévêque, and A. Akjouj, "Lspr in plasmonic nanostructures: theoretical study with application to sensor design", in *Encyclopedia of nanotechnology*, edited by B. Bhushan (Springer Netherlands, Dordrecht, 2016), pp. 1–8.

[10] G. Mie, "Beiträge zur optik trüber medien, speziell kolloidaler metallösungen", Annalen der physik **330**, 377–445 (1908).

[11] C. Langhammer, Z. Yuan, I. Zorić, and B. Kasemo, "Plasmonic properties of supported pt and pd nanostructures", Nano letters **6**, 833–838 (2006).

[12] C. F. Bohren and D. R. Huffman, *Absorption and scattering of light by small particles* (John Wiley & Sons, 2008).

[13] S. A. Maier, *Plasmonics: fundamentals and applications* (Springer Science & Business Media, 2007).

[14] F. Manchester, A. San-Martin, and J. Pitre, "The h-pd (hydrogen-palladium) system", Journal of phase equilibria **15**, 62–83 (1994).

[15] K. Young, "Metal hydrides", in *Reference module in chemistry, molecular sciences and chemical engineering* (Elsevier, 2018).
[16] F. A. A. Nugroho, "Nanoplasmonic alloy hydrogen sensors", PhD thesis (Chalmers Tekniska Hogskola (Sweden), 2018).
[17] C. Wadell, F. A. A. Nugroho, E. Lidström, B. Iandolo, J. B. Wagner, and C. Langhammer, "Hysteresis-free nanoplasmonic pd–au alloy hydrogen sensors", Nano letters **15**, 3563–3570 (2015).
[18] P. Erhart and M. Rahm, *Alloy dielectric functions*, `https://sharc.materialsmodeling.org/alloy_dielectric_functions/` (2020 (accessed February 18, 2020)).
[19] H. Fredriksson, Y. Alaverdyan, A. Dmitriev, C. Langhammer, D. S. Sutherland, M. Zäch, and B. Kasemo, "Hole–mask colloidal lithography", Advanced Materials **19**, 4297–4302 (2007).
[20] F. A. Nugroho, B. Iandolo, J. B. Wagner, and C. Langhammer, "Bottom-up nanofabrication of supported noble metal alloy nanoparticle arrays for plasmonics", ACS nano **10**, 2871–2879 (2016).
[21] T. J. Antosiewicz, S. P. Apell, M. Zäch, I. Zorić, and C. Langhammer, "Oscillatory optical response of an amorphous two-dimensional array of gold nanoparticles", Physical review letters **109**, 247401 (2012).

# A

# Appendix 1

## A.1 Matlab Scripts and Functions Used for Simulations

### A.1.1 Script Used for Comparing Simulations and Experimental Results

```
%% Code that calculates the LSPR response before and after hydrogen formation,
% and evaluates the change in extinction cross section as a function of
% wavelength in order to find the optimal and non-optimal sensing regions.
%%
clear all
close all
clc

% EXPERIMENTAL: 4% H2 vs 0% H2

% Loading experimental data
filename_0="wavelength.txt";

filename_1="210nm_2080_annealedatannreactor_20h_500C_april7_2ndmeas_
lowerconc export_0percH2_4.txt";
filename_2="210nm_2080_annealedatannreactor_20h_500C_april7_2ndmeas_
lowerconc export_4percH2.txt";


filename_210_4H2=[filename_1, filename_2];

for i=1:length(filename_210_4H2)
    A_210_4H2(i)=importdata(filename_210_4H2(:,i));
    sigma_ext_210_4H2(:,i)=A_210_4H2(i).data;
end

% Wavelength
lambda_exp=importdata(filename_0);

% 1048 gives 700 nm
```

```
% 1003 gives 685 nm
% 445 gives 500 nm

% Choosing data between 500-1000 nm
sigma_ext_210_4H2_short=sigma_ext_210_4H2(445:1984,:);
lambda_exp_short=lambda_exp(445:1984);

% SIMULATIONS
a=105;        % Radius of the disk in the x-direction
b=a;          % Radius of the disk in the y-direction
c=12.5;       % Radius of the disk in the z-direction


fex= @(x) 1./((a^2+x).*sqrt((x+a^2).*(x+b^2).*(x+c^2))); % Integrand
for shape parameter of NP (x- and y-direction)
Lex=(a*b*c/2).*quadgk(fex,0,inf); % Calculation of the shape parameter
for nanoparticle (x- and y-directions)


% Importing and sorting data

% Pd80Au20
filename="Pd_80.00_Au_20.00.txt";

A=importdata(filename);

% Extracting data
data_Au20=A.data;

% Extracting the wavelength (lambda), real part of the dielectric
function (epsilon_Re),
% imaginary part of the dielectric function (epsilon_Im), real part
of refractive index (n_Re),
% imaginary part of refractive index (n_Im) and EELS spectrum (EELS)
for the different alloys.

maxlambda=151; % approximately 2500 nm (For 1000 use 137)

lambda(:,1)=data_Au20(1:maxlambda,1);
epsilon_Re=data_Au20(1:maxlambda,2);
epsilon_Im=data_Au20(1:maxlambda,3);
n_Re=data_Au20(1:maxlambda,4);
n_Im=data_Au20(1:maxlambda,5);
EELS=data_Au20(1:maxlambda,6);
```

```
% Defining the polarizability and finding its poles

% Constructing the complex dielectric function of the alloy
for m=1:length(filename)
    epsilon(:,m)=epsilon_Re(:,m)+1i*epsilon_Im(:,m);
end


%V1=4*pi*a*b*c/3;  % Volume of the NP (Spheroid)
V1=(pi*(2*a)^2)*2*c/6; % Volume of the NP (Disk)

n=1.26;          % Refractive index of the surrounding medium. For air, use n=1.
                 % For glass, use n=1.52. For NP in air, on a glass
                 % substrate, use n=1.26 (average).

% Calculating the complex polarizability of the NPs for different aspect ratios

alpha_Au20=V1.*(epsilon(:,1)-n^2)./(n^2+Lex.*(epsilon(:,1)-n^2));

% Correcting the polarizability and calculating the extinction cross-section

d=2*a; % Disc diameter

k=2*pi./lambda; % Wave "vector"

% Corrected polarizability
alpha_corr_Au20=alpha_Au20./(1-1i*k.^3.*alpha_Au20./(6*pi)-k.^2.*
alpha_Au20./(2*pi*d));


% Extinction cross-section
sigma_ext_Au20=k.*imag(alpha_corr_Au20);

sigma_scatter=k.^4/(9*pi).*abs(alpha_corr_Au20).^2;
sigma_abs=sigma_ext_Au20;

sigma_Ext_Au20=sigma_abs+sigma_scatter;

% Fitting the extinction cross-section of the nanoparticle
(d=210 nm and h=25 nm) to a 3-term gaussian
% function, for n=1.26
sigma_fit=fit(lambda, sigma_Ext_Au20,'gauss3');

% Result:
% Coefficients:
a1=sigma_fit.a1;
```

```
a2=sigma_fit.a2;
a3=sigma_fit.a3;
b1=sigma_fit.b1;
b2=sigma_fit.b2;
b3=sigma_fit.b3;
c1=sigma_fit.c1;
c2=sigma_fit.c2;
c3=sigma_fit.c3;

x=linspace(100,2500,1201);

val1=a1*exp(-((x-b1)/c1).^2)+a2*exp(-((x-b2)/c2).^2)+a3*exp(-((x-b3)/c3).^2);
%val1=a1*exp(-((x-b1)./c1).^2); % Calculating the fit

peak_1=max(val1); % Maximum (peak) value of the fitted Gaussian for n=1.26

% Assigning the peak value to the corresponding wavelengths
for i=1:700
    if val1(i)==peak_1
        lambdapeak_1=2*i+100;
    end
end

% Simulating 4% H2 by updated refractive index
n_min=1.26; % Lower boundary of n
n_max=1.35; % Upper boundary of n
steps=91; % Amount of steps

%%
% Calculating the peakshift using newrefrac function.
[deltalambda_peak, n_ny, lambdapeak_2, peak_2]=newrefrac(V1, epsilon, Lex,
a, lambda, n_min, n_max, lambdapeak_1, x, steps);

%%
% Using the n_ny that gives a peakshift of 26nm. (n=1.32)
n_new=n_ny(1,61); % "New" refractive index of surrounding medium
(simulating hydrogen present)

alpha_Au20_n=V1.*(epsilon(:,1)-n_new^2)./(n_new^2+Lex
.*(epsilon(:,1)-n_new^2));

alpha_corr_Au20_n=alpha_Au20_n./(1-1i*k.^3.*alpha_Au20_n./(6*pi)-k.^2.
*alpha_Au20_n./(2*pi*d));

sigma_ext_Au20_n=k.*imag(alpha_corr_Au20_n);
```

```
sigma_scatter_n=k.^4/(9*pi).*abs(alpha_corr_Au20_n).^2;
sigma_abs_n=sigma_ext_Au20_n;

sigma_Ext_Au20_n=sigma_abs_n+sigma_scatter_n;

% Fitting the new response

sigma_fit_n=fit(lambda, sigma_Ext_Au20_n,'gauss3');

a1_n=sigma_fit_n.a1;
a2_n=sigma_fit_n.a2;
a3_n=sigma_fit_n.a3;
b1_n=sigma_fit_n.b1;
b2_n=sigma_fit_n.b2;
b3_n=sigma_fit_n.b3;
c1_n=sigma_fit_n.c1;
c2_n=sigma_fit_n.c2;
c3_n=sigma_fit_n.c3;

val1_n=a1_n*exp(-((x-b1_n)/c1_n).^2)+a2_n*exp(-((x-b2_n)/c2_n).^2)
+a3_n*exp(-((x-b3_n)/c3_n).^2);

% Extinction difference due to new n (4% H2) for 25nm height
%diff_sigma_ext=abs(sigma_ext_Au20-sigma_ext_Au20_n);

diff_sigma_ext=abs(val1-val1_n);

diff_sigma_ext_exp=abs(sigma_ext_210_4H2_short(:,1)
-sigma_ext_210_4H2_short(:,2));
diff_sigma_ext_exp_full=abs(sigma_ext_210_4H2(:,1)
-sigma_ext_210_4H2(:,2));

%% Plotting

figure(1)
yyaxis right
plot(lambda_exp_short,sigma_ext_210_4H2_short(:,1))
hold on
plot(lambda_exp_short,sigma_ext_210_4H2_short(:,2))
ylabel('Extinction')
ylim([0.1 0.295])
yyaxis left
plot(lambda,sigma_Ext_Au20)
plot(lambda,sigma_Ext_Au20_n)
ylabel('Extinction cross-section')
xlabel('Wavelength [nm]')
```

```
legend('Simulation 0% H2', 'Simulation 4% H2', 'Experimental 0% H2'
, 'Experimental 4% H2')
hold off

figure(2)
yyaxis right
plot(lambda_exp_short, diff_sigma_ext_exp)
hold on
ylabel('Extinction difference')
%ylim([0.1 0.31])
yyaxis left
plot(x,diff_sigma_ext)
ylabel('Extinction cross-section difference')
xlabel('Wavelength [nm]')
legend('Simulation 0% vs 4% H2', 'Experimental 0% vs 4% H2')
hold off

figure(3)
yyaxis right
plot(lambda_exp_short,sigma_ext_210_4H2_short(:,1))
hold on
plot(lambda_exp_short,sigma_ext_210_4H2_short(:,2))
ylabel('Extinction')
ylim([0.1 0.295])
yyaxis left
plot(x,val1)
plot(x,val1_n)
ylabel('Extinction cross-section')
xlabel('Wavelength [nm]')
legend('Simulation 0% H2', 'Simulation 4% H2', 'Experimental 0% H2'
, 'Experimental 4% H2')
hold off
```

### A.1.2 Function (newrefrac) Used in the A.1.1 Script

```
function [deltalambda_peak_ny, n_ny, lambdapeak_2, peak_2] =
newrefrac(V1, epsilon, Lex, a, lambda, n_min, n_max, lambdapeak_1, x, steps)

n_ny=linspace(n_min,n_max, steps);
% Calculating the complex polarizability of the NPs for different
aspect ratios

for j=1:length(n_ny)
    alpha_Au20_ny=V1.*(epsilon(:,1)-n_ny(j)^2)./(n_ny(j)^2+Lex.
    *(epsilon(:,1)-n_ny(j)^2));
```

```
% Correcting the polarizability and calculating the extinction
cross-section

d=2*a; % Disc diameter

k=2*pi./lambda; % Wave "vector"

% Corrected polarizability
alpha_corr_Au20_ny=alpha_Au20_ny./(1-1i*k.^3.*alpha_Au20_ny./(6*pi)
-k.^2.*alpha_Au20_ny./(2*pi*d));


% Extinction cross-section
sigma_ext_Au20_ny=k.*imag(alpha_corr_Au20_ny);
sigma_scatter_ny=k.^4/(9*pi).*abs(alpha_corr_Au20_ny).^2;
sigma_abs_ny=sigma_ext_Au20_ny;

sigma_Ext_Au20_ny=sigma_abs_ny+sigma_scatter_ny;


% Fitting the extinction cross-section of the nanoparticle
(d=210 nm and h=25 nm) to a 3-term gaussian
% function, for n=1.26
sigma_fit=fit(lambda, sigma_Ext_Au20_ny,'gauss3');

% Result:
% Coefficients:
a1_ny=sigma_fit.a1;
a2_ny=sigma_fit.a2;
a3_ny=sigma_fit.a3;
b1_ny=sigma_fit.b1;
b2_ny=sigma_fit.b2;
b3_ny=sigma_fit.b3;
c1_ny=sigma_fit.c1;
c2_ny=sigma_fit.c2;
c3_ny=sigma_fit.c3;

% Calculating the fit
val2=a1_ny*exp(-((x-b1_ny)/c1_ny).^2)+a2_ny*exp(-((x-b2_ny)/c2_ny)
.^2)+a3_ny*exp(-((x-b3_ny)/c3_ny).^2);


peak_2(j)=max(val2(129:1201)); % Maximum (peak) value of the fitted
Gaussian for n=n_test
```

```
    % Assigning the peak values to their corresponding wavelengths
    for i=129:1200 % Excluding wavelengths below 766nm
    (Peak wavelength for n=1.26)
        if val2(i)==peak_2(j)
            lambdapeak_2(j)=2*i+100;
        end
    end

    % Peak shift
    deltalambda_peak_ny(j)=lambdapeak_2(j)-lambdapeak_1;
end

end
```

### A.1.3 Script for Calculation of LSPR Response from Differently Alloyed Nanoparticles

```
%% Nanodisk plasmonics
% This code calculates the shape parameters in the x- and
z-directions of disk-shaped
% nanoparticles, approximated as oblate spheroids. It then imports
data for different PdAu
% alloys, includig the dielectric function (complex permittivity).
Using the complex
% dielectric function, it then calculate the polarizability
(in the quasistatic approximation)
% of the nanoparticles, as a function of the wavelength of
incoming light. The result is plotted
% for the different compositions. Different sizes and aspect ratios
are also possible to simulate
% by changing these parameters accordingly.

%% Calculation of shape parameter
clc
clear all
clf

a=265;        % Radius of the disk in the x-direction
b=265;        % Radius of the disk in the y-direction
c=10;       % Radius of the disk in the z-direction

fz = @(x) 1./((c^2+x).*sqrt((x+a^2).*(x+b^2).*(x+c^2))); % Integrand
for shape parameter of NP (z-direction)
fx= @(x) 1./((a^2+x).*sqrt((x+a^2).*(x+b^2).*(x+c^2))); % Integrand
for shape parameter of NP (x- and y-direction)
```

```
Lz=(a*b*c/2)*quadgk(fz,0,inf); % Calculation of the shape parameter
for nanoparticle (z-direction)
Lx=(a*b*c/2)*quadgk(fx,0,inf); % Calculation of the shape parameter
for nanoparticle (x- and y-directions)

%% Importing and sorting data

% Pd
filename_Au0="Pd_100.00_Au_0.00.txt";

%Pd75Au25
filename_Au25="Pd_75.00_Au_25.00.txt";

% Pd70Au30
filename_Au30="Pd_70.00_Au_30.00.txt";

% Pd65Au35
filename_Au35="Pd_65.00_Au_35.00.txt";

% Pd50Au50
filename_Au50="Pd_50.00_Au_50.00.txt";

% Au
filename_Au100="Pd_0.00_Au_100.00.txt";

filename=[filename_Au0, filename_Au25, filename_Au30, filename_Au35,
filename_Au50, filename_Au100];

for i=1:length(filename)
    A(i)=importdata(filename(:,i));
end

%% Extracting data

% Sorting data after their Au content
data_Au0=A(1).data;
data_Au25=A(2).data;
data_Au30=A(3).data;
data_Au35=A(4).data;
data_Au50=A(5).data;
data_Au100=A(6).data;


% Extracting the wavelength (lambda), real part of the dielectric
function (epsilon_Re),
% imaginary part of the dielectric function (epsilon_Im), real part
```

```
of refractive index (n_Re),
% imaginary part of refractive index (n_Im) and EELS spectrum
(EELS) for the different alloys.
maxlambda=151; % approximately 2500 nm

lambda(:,1)=data_Au0(1:maxlambda,1);
epsilon_Re=[data_Au0(1:maxlambda,2),
data_Au25(1:maxlambda,2), data_Au30(1:maxlambda,2),
data_Au35(1:maxlambda,2),
data_Au50(1:maxlambda,2), data_Au100(1:maxlambda,2)];
epsilon_Im=[data_Au0(1:maxlambda,3),
data_Au25(1:maxlambda,3), data_Au30(1:maxlambda,3),
data_Au35(1:maxlambda,3), data_Au50(1:maxlambda,3),
data_Au100(1:maxlambda,3)];
n_Re=[data_Au0(1:maxlambda,4), data_Au25(1:maxlambda,4),
data_Au30(1:maxlambda,4), data_Au35(1:maxlambda,4),
data_Au50(1:maxlambda,4), data_Au100(1:maxlambda,4)];
n_Im=[data_Au0(1:maxlambda,5), data_Au25(1:maxlambda,5),
data_Au30(1:maxlambda,5), data_Au35(1:maxlambda,5),
data_Au50(1:maxlambda,5), data_Au100(1:maxlambda,5)];
EELS=[data_Au0(1:maxlambda,6), data_Au25(1:maxlambda,6),
data_Au30(1:maxlambda,6), data_Au35(1:maxlambda,6),
data_Au50(1:maxlambda,6), data_Au100(1:maxlambda,6)];

%% Defining the polarizability and finding its poles

% Constructing the complex dielectric function of the alloy
for m=1:6
    epsilon(:,m)=epsilon_Re(:,m)+1i*epsilon_Im(:,m);
end


%V=4*pi*a*b*c/3;  % Volume of the NP (Spheroid)
V=(pi*(2*a)^2)*2*c/6; % Volume of the NP (Disk)

n=1.26;          % Refractive index of the surrounding medium.
                 % For air, use n=1.
                 % For glass, use n=1.52. For NP in air, on a glass
                 % substrate, use n=1.26 (average).

% Calculating the complex polarizability of the NP
alpha=V*(epsilon-n^2)./(n^2+Lx*(epsilon-n^2));

d=2*a;

k=2*pi./lambda;
```

```
alpha_corr=alpha./(1-1i*k.^3.*alpha./(6*pi)-k.^2.*alpha./(2*pi*d));

sigma_ext=k.*imag(alpha_corr);

sigma_scatter=k.^4/(9*pi).*abs(alpha_corr).^2;
sigma_abs=sigma_ext;

sigma_Ext=sigma_abs+sigma_scatter;


%% Finding maximas

lambdasigma=[lambda, sigma_ext];

% Maximas of sigma_ext
realmax=max(sigma_ext);

for i=1:6
    for j=1:length(lambda)
        if lambdasigma(j,i+1)==realmax(i)
            maximum(i,1)=lambdasigma(j,1);
            maximum(i,2)=lambdasigma(j,i+1);
        end
    end
end

%% Plotting only Pd

figure(1)
for n=1
    plot(lambda, sigma_Ext(:,n))
    hold on
    plot(lambda, sigma_ext(:,n))
    %plot(maximum(n,1),maximum(n,2),'*')
end
legend('Pd')
xlabel('Wavelength nm')
ylabel('Extinction cross-section')
title('Extinction spectrum with maxima')
hold off
```

## A.2 Matlab Scripts for Evaluation of Experiments in the Reactor and the LUFT-device

### A.2.1 Script for Visualising Experimental Data from the LUFT-device or the Reactor

```
% Importing data
clear all
clc
clf

filename1="Test200529_H2test_650.txt"; % Insert desired filename

% Key to data file (data in respective columns):
% t[s] TBrd[Deg] TA[Deg] TB[Deg] SigA[rel] CurA[rel]
SigB[rel] CurB[rel] SigA/B[rel] Raw[mil] Tcmp[mil]
TcR[mil] Base[cal] SNow[cal] Sfilt[cal] Sig[cal]
Te[Deg] Sdv[mil]

Data=importdata(filename1); % Importing data
%% Data extraction

for i=1:18 % number of columns, 18 for 200507, 200522 and 200525,
13 for 200420, 26 for 200520, 18 for 200522, 24 for the others

    Channels(:,i)=Data.data(:,i);
end


% Time: Column 1
t=Channels(:,1);

% TcR: Column 12 for 200507, 200522 and 200525, 11 for 200420,
20 for the others

Sig_TcR=Channels(:,12);
Raw=Channels(:,10);

%% Baseline correction - Use only for the Test200420_H2test_Horus7105
yOut=msbackadj(t,-Sig_TcR,'WindowSize',1000);

%% Plotting

figure(1)
plot(t, Sig_TcR)
```

```
%hold on
%plot(t,Raw)
%plot(t(1:15360), baseline)
xlabel('Time [s]')
ylabel('[mil]')
title('Relative signal ')
```

### A.2.2 Function (absoluteShift) Used to Extract Changes in Extinction and Transmission

```
function [a] = absoluteShift(v,m,n)
%v = parameter that you want to extract m and n is the data point

a = zeros(m,n);

%tid = time;

for i = 1:m

for j = 1:n

scrsz = get(0,'ScreenSize')
ransel = figure('Position',[scrsz(3)/10 scrsz(4)/10 scrsz(3)*8/10 scrsz(4)*8/10],
'Name',['Cycle ' int2str(j)] )
plot(v);title('Select range');
[range,y]=ginput(2);
range = ceil(min(range)):floor(max(range));

plot(v(range));
[x,skalav]=ginput(2);

a(i,j) = max(skalav)-min(skalav);
close(ransel)
end
end

%mean(thalv)
%std(thalv)
```

### A.2.3 Calibration Curve Constructing Script

```
%% Calibration curve construction single measurements 940 nm or 650 nm

clc
clear all
clf
```

```
% Loading the extinction changes collected using the
% absoluteShift function from LUFT data

% 0.01%
perc_001_650=load('0comma01%Test200529H2test.mat').shift;
perc_001_940=load('0comma01%Test200601H2test.mat').shift;

% 0.1%
perc_01_650=load('0comma1%Test200529H2test.mat').shift;
perc_01_940=load('0comma1%Test200601H2test.mat').shift;

% 0.5%
perc_05_650=load('0comma5%Test200529H2test.mat').shift;
perc_05_940=load('0comma5%Test200601H2test.mat').shift;

% 1%
perc_1_650=load('1%Test200529H2test.mat').shift;
perc_1_940=load('1%Test200601H2test.mat').shift;

% 4%
perc_4_650=load('4%Test200529H2test.mat').shift;
perc_4_940=load('4%Test200601H2test.mat').shift;

% 650 nm
% Means
mean_001_650=mean(perc_001_650);
mean_01_650=mean(perc_01_650);
mean_05_650=mean(perc_05_650);
mean_1_650=mean(perc_1_650);
mean_4_650=mean(perc_4_650);

% Standard deviations
std_001_650=std(perc_001_650);
std_01_650=std(perc_01_650);
std_05_650=std(perc_05_650);
std_1_650=std(perc_1_650);
std_4_650=std(perc_4_650);


% 940 nm
% Means
mean_001_940=mean(perc_001_940);
mean_01_940=mean(perc_01_940);
mean_05_940=mean(perc_05_940);
mean_1_940=mean(perc_1_940);
```

```
mean_4_940=mean(perc_4_940);

% Standard deviations
std_001_940=std(perc_001_940);
std_01_940=std(perc_01_940);
std_05_940=std(perc_05_940);
std_1_940=std(perc_1_940);
std_4_940=std(perc_4_940);


%% PLOTTING calibration curves for single measurements 940 nm and 650 nm

conc=[0.01 0.1 0.5 1 4];

% Measurement 1

signal_650=[mean_001_650 mean_01_650 mean_05_650 mean_1_650 mean_4_650];
err650=[std_001_650 std_01_650 std_05_650 std_1_650 std_4_650];

% Measurement 2

signal_940=[mean_001_940 mean_01_940 mean_05_940 mean_1_940 mean_4_940];
err940=[std_001_940 std_01_940 std_05_940 std_1_940 std_4_940];


figure(1)
%semilogx(conc, signal_1)
errorbar(conc,signal_650, err650, 'b-')
hold on
%semilogx(conc, signal_2)
%semilogx(conc, signal_3)
errorbar(conc,signal_940,err940, 'r-')
xlabel('H_2 concentration [%]')
ylabel('Relative signal [mil]')
legend('650 nm LEDs', '940 nm LEDs')
set(gca, 'xscale', 'log')
```